Responses to the Editor

Dear Authors,

Thank you for the responses to the reviewers' comments. I am still not convinced that you have addressed the first point regarding the altitude dependence and the applicability of the HCHO/NO2 column ratio to infer chemical regimes and its change beyond the strong ozone production region. You mentioned that you have conducted additional ozone sensitivity analysis, which is to be presented in another paper that is being prepared. I would encourage you to include the main results of that analysis in the manuscript to support your statement. 'In preparation' papers cannot be cited - unless available as preprints through an archival repository. Please add the salient analysis from the manuscript under preparation in the supplementary text to support this.

We thank the editor for his time and effort in reviewing our article. Please find below our answers in blue following each comment.

Answer: Regarding the reviewer's comment on the altitude dependencies of the HCHO/NO2 ratio, we didn't look into that. So, we can't comment on that from the measurement point of view. However, from the model simulation in Figure 5, the mean (2005-2019) percent contribution from the upper versus lower troposphere differs between HCHO and NO_2, both globally and in the tropical band, leading to a lower HCHO/NO2 ratio in the upper troposphere relative to the middle and lower troposphere. The lower HCHO/NO2 ratio in the upper troposphere is due to the lower photochemically formed HCHO mixing ratios, consistent with other studies (Souri et al., 2023; Müller et al., 2024). However, delving into the altitude dependence of the HCHO/NO2 would require an additional significant space/effort and is not

among the objectives of this global study and it has been addressed in many other regional studies (e.g., Souri et al., 2023; Chong et al., 2024; Müller et al., 2024).

Regarding the regional trends in HCHO/NO2 ratio, our analysis in section 3.4.7 is indeed limited to ozone production sites, e.g., in Eastern Asia, North America, Europe, and the tropics.

The sensitivity paper will be submitted very soon, but the citation might take a couple of weeks to appear, therefore, we removed the citation to this article from the references list. The sensitivity paper was mentioned in our response to the reviewers but not in the body of this article. However, I have included here a confidential version of a draft of this article for your reference.

Another point is the format of the references. Please use the Copernicus reference formatting style throughout the reference list - there are many instances of wrong formatting being used.

Answer: The format of the references is fixed now.

References:

Chong, K., Wang, Y., Liu, C., Gao, Y., Boersma, K. F., Tang, J., & Wang, X. (2024). Remote sensing measurements at a rural site in China: Implications for satellite NO2 and HCHO measurement uncertainty and emissions from fires. Journal of Geophysical Research: Atmospheres, 129, e2023JD039310. https://doi.org/10.1029/2023JD039310, 2024.

Müller, J.-F., Stavrakou, T., Oomen, G.-M., Opacka, B., De Smedt, I., Guenther, A., Vigouroux, C., Langerock, B., Aquino, C. A. B., Grutter, M., Hannigan, J., Hase, F., Kivi, R., Lutsch, E., Mahieu, E., Makarova, M., Metzger, J.-M., Morino, I., Murata, I., Nagahama, T.,

Notholt, J., Ortega, I., Palm, M., Röhling, A., Stremme, W., Strong, K., Sussmann, R., Té, Y., and Fried, A.: Bias correction of OMI HCHO columns based on FTIR and aircraft measurements and impact on top-down emission estimates, Atmos. Chem. Phys., 24, 2207–2237, https://doi.org/10.5194/acp-24-2207-2024, 2024.

Souri, A. H., Johnson, M. S., Wolfe, G. M., Crawford, J. H., Fried, A., Wisthaler, A., Brune, W. H., Blake, D. R., Weinheimer, A. J., Verhoelst, T., Compernolle, S., Pinardi, G., Vigouroux, C., Langerock, B., Choi, S., Lamsal, L., Zhu, L., Sun, S., Cohen, R. C., Min, K.-E., Cho, C., Philip, S., Liu, X., and Chance, K.: Characterization of errors in satellite-based HCHO$/$NO$_2$ tropospheric column ratios with respect to chemistry, column-to-PBL translation, spatial representation, and retrieval uncertainties, Atmos. Chem. Phys., 23, 1963–1986, https://doi.org/10.5194/acp-23-1963-2023, 2023.

Wang, Y., Dörner, S., Donner, S., Böhnke, S., De Smedt, I., Dickerson, R. R., Dong, Z., He, H., Li, Z., Li, Z., Li, D., Liu, D., Ren, X., Theys, N., Wang, Y., Wang, Y., Wang, Z., Xu, H., Xu, J., and Wagner, T.: Vertical profiles of NO$_2$, SO$_2$, HONO, HCHO, CHOCHO and aerosols derived from MAX-DOAS measurements at a rural site in the central western North China Plain and their relation to emission sources and effects of regional transport, Atmos. Chem. Phys., 19, 5417–5449, https://doi.org/10.5194/acp-19-5417-2019, 2019.

1

Influence of nitrogen oxides and volatile organic compounds emission changes on

tropospheric ozone variability, trends and radiative forcing

Suvarna Fadnavis[1], Yasin Elshorbany[2], Brice Barret[3], Jerald Ziemke[4], Alexandru Rap[5], Satheesh Chandran PR[1], Richard J. Pope[5], Vijay Sagar[1], Domenico Taraborrelli[6], Eric Le Flochmoe[3], Juan Cuesta[7], Catherine Wespes[8], Folkert Boersma[9,10], Isolde Glissenaar[9], Isabelle De Smedt[11],Michel Van Roozendael[11], Hervé Petetin[12],

[1]Center for Climate Change Research, Indian Institute of Tropical Meteorology, MoES, Pune, India
[2]School of Geosciences, College of Arts and Sciences, University of South Florida, St. Petersburg, FL, USA
[3]LAERO/OMP, Université Paul Sabatier, Université de Toulouse-CNRS, Toulouse, France
[4]NASA Goddard Space Flight Center, Greenbelt, Maryland, USA
[5]School of Earth and Environment, University of Leeds, Leeds, UK
[6]Institute of Energy and Climate Research, IEK-8: Troposphere, Forschungszentrum Jülich GmbH, Jülich, Germany,
[7]University Paris Est Creteil and Université Paris Cité, CNRS, LISA, F-94010 Créteil, France
[8]Université libre de Bruxelles (ULB), Spectroscopy, Quantum Chemistry and Atmospheric Remote Sensing, Brussels, Belgium
[9]Royal Netherlands Meteorological Institute (KNMI), De Bilt, The Netherlands
[10]Wageningen University, Environmental Sciences Group, Wageningen, The Netherlands
[11]Belgian Institute for Space Aeronomy
[12]Barcelona Supercomputing Center, Barcelona, Spain

Corresponding author email: suvarna@tropmet.res.in

Abstract:

Ozone in the troposphere is a prominent pollutant whose production is sensitive to the emissions of nitrogen oxides (NOx) and volatile organic compounds (VOC). In this study, we assess the variation of tropospheric ozone levels, trends, ozone photochemical regimes and radiative effect using the ECHAM6-HAMMOZ chemistry-climate model which is validated against satellite measurements. Further, we investigate the impacts of doubling/halving NO_X (DNOx/HNOx) and VOC (DVOC/HVOC) emissions on ozone levels, trends, ozone photochemical regimes, and radiative effect. Our analysis shows that the enhancement in global mean tropospheric column ozone (TCO) is sixteen times higher in DNOx (mean:11.7, [minimum: 5.6; maximum:29.3 ppb]) than in DVOC (0.7 [-0.5; 3.6] ppb) simulations. The decrease (increase) in surface ozone with the increase in NOx (VOC) in DNOx (DVOC) simulation indicates the prevalence of VOC-limited regime over Indo-Gangetic Plains, Eastern China, Eastern US, and Europe.

The estimated global mean trends in TCO show increasing tendencies in OMI/MLS (1.4 [-2.1; 4.5] ppb.decade^{-1} from January 2005 to December 2020), IASI-SOFRID (0.08 [-3.9; 7.1] from 2008 to 2020), and ECHAM6-HAMMOZ model simulations (0.9 [-0.9; 4.5] ppb.decade^{-1} from 1998 to 2020). The global mean trend in TCO is increasing in DNOx (2.2 [-1.5; 6.2] ppb.decade^{-1}) and DVOC (1.4 [-0.2; 5.8] ppb.decade^{-1}) compared to control (CTL) simulations. However, trends are negative in DNOx-CTL over India and China (-1.2 to 4.7 ppb.decade^{-1}) and in the DVOC-CTL simulation over Africa and Europe (0.7 to 4.2 sppb.decade^{-1}).

The model simulations show nonlinear enhancement in surface ozone over Australia, Amazon Argentina, and the southwest part of Indo-China in response to changes in NOx and VOC emissions. The simulations show VOC-limited regimes over Indo-Gangetic Plains, Eastern China, Western Europe and the eastern part of the US in DNOx, while in HNOx, America and Asia become NOx-limited. In DVOC simulations, spatial extent of VOC-limited regimes decreased over Eastern China and Western Europe.

Further, we provide estimates of tropospheric ozone radiative effects (TO3RE). Estimated global mean TO3RE is 1.21 $W.m^{-2,}$ during 1998-2020 which is enhanced in DNOX-CTL (by 0.36 $W.m^{-2}$) and DVOC-CTL (by 0.01 and reduced in HNOx (by -0.12 $W.m^{-2}$) and HVOC-CTL (by -0.03 $W.m^{-2}$) simulations. We show that the global troposphere in the last 25 years is mostly NOx-limited, and show increasing trends. The anthropogenic NOx emissions have a higher impact on radiative forcing than VOC emissions globally.

1. Introduction

Tropospheric ozone, a major air pollutant, has been a pressing issue in recent decades due to its detrimental effect on human and ecosystem productivity and as a short-term climate forcer (IPCC, 2021; Wang et al., 2022). Considering these harmful impacts, the assessment of tropospheric ozone levels and trends is being conducted frequently (Mills et al., 2018; Gaudel et al., 2018, Tarasick et al., 2019). Ozone trends are being assessed from surface observations, in-situ and ground-based measurements, satellite retrievals, and model simulations (Cooper et al., 2014; Tarasick et al., 2018; Cohen et al., 2018). The numbers of Tropospheric Ozone Assessment Reports (TOAR) (Cooper et al 2014; Schultz et al., 2017; Young et al., 2018; Fleming et al., 2018; Lefohn et al.,

73   2018; Gaudel et al., 2018; Mills et al., 2019; Tarasick et al., 2019) have documented global

74   increases of tropospheric column ozone (TCO) over the course of the 20th century. Increasing

75   tropospheric trends are explained by enhanced anthropogenic emissions (Cooper et al., 2014,

76   Zhang et al., 2016) and modulation by climate variability (Lin et al 2014, Lu et al., 2018). Several

77   studies documented an increase in trends in TCO e.g 2%–7% per decade in the northern mid-

78   latitudes, 2%–12% in the tropics (Gulev et al 2021), 5–20 % during 1970 to 1995 over Canada

79   (Tarasick et al., 2019), 2.7 ± 1.7 and 1.9 ± 1.7 ppb per decade during 1995–2017 over globe from

80   multiple observations (Global Observing System database (IAGOS), ozone sondes), and a multi-

81   decadal GEOS-Chem chemical model simulation (Wang et al., 2022), 0.6 to 2.5 ppb.decade^{-1}

82   during 1950-2014 from the IAGOS measurements and CESM2-WACCM6 model (Fiore et al.,

83   2022). Trends in TCO are stronger in the Northern Hemisphere (NH) than Southern Hemisphere

84   (SH) due to larger anthropogenic emissions (Monks et al., 2015). Ozone Monitoring Instrument

85   (OMI) and Microwave Limb Sounder (MLS) observations from 2005 until 2010 show annual TCO

86   trends averaged over the NH exceed the SH average by 4% at low (0°–25°), by 12% at mid (25°–

87   50°), and by 18% at high (50°–60°) latitudes (Cooper et al., 2014).

88

89   The trends in surface ozone have grown during the last century, however, a few locations

90   show decreasing trends (Cooper et al., 2014). The UKESM1 model simulations show that global

91   mean surface ozone increased by ~28% throughout the twentieth century. The set of lower

92   tropospheric and surface ozone measurements in the NH shows an increase in ozone by 30%–70%

93   since the middle of the 20th Century (Gulev et al., 2021). Recent observations from UV-absorption

94   analyzers in Southwestern Europe from 2000–2021 show an increase in ozone trends of 2.2 ± 0.3

95   ppb.decade^{-1} (Adame et al., 2022). However, some of the station data showed negative trends in

96   surface ozone during 1980–2001, for example, Goose Bay, Labrador (-0.7 ± 0.4 ppb.decade^{-1}),

97   Churchill, Manitoba, (-0.6 ± 0.4 ppb.decade^{-1}), Edmonton, Alberta (-1.4 ± 0.7 ppb.decade^{-1})

98   (Adame et al.2022). Cooper et al., (2014) reported that surface ozone trends have varied over

99   different regions from 1990 until 2010. In Western Europe, ozone concentration increased in the

100   1990s, followed by a leveling off or decrease since 2000. Analysis of worldwide monthly surface

101   ozone anomaly data from 2000 to 2018 shows the strongest negative trend of -2.8 ± 1.1

102   ppb.decade^{-1} at Gothic station (41°N, 2.1°E) and strongest positive trend of 2.2 ± 0.9 ppb.decade^{-1}

103   at American Samoa (14°S, 171°W) (Cooper et al., 2020). Lu et al. (2019) reported surface ozone

104   trends varying between 0.17 % to 0.81 % in the SH from 1990 to 2015.

105

106   Ozone trends are influenced by the emission of its precursor gasses. In order to

107   comprehensively address the observed ozone trends and photochemical regimes, it is imperative

108   to gain a deeper understanding of the levels of major ozone precursor gasses, namely nitrogen

109   oxide (NOx) and Volatile Organic Compounds (VOCs). The levels of these ozone precursor gasses

110   vary due to changes in economic activities, natural variability, and due to various pollution control

111   strategies being implemented. In Europe, a reduction of emissions of ozone precursor (HCHO,

112   CO, NO$_2$) by 27-32% in the past decade (2002-2011) has led to an overall decline in surface ozone

113   levels (Guerreiro et al., 2014). Over the US, a decline in NOx by 38%, VOC by 17%, and CO by

114   67% during the period 2000-2022 has resulted in a reduction in the national average surface ozone

115   levels by ~17% (EPA 2023). Conversely, Southeast Asia has witnessed a decrease in NOx by 3%

116 and VOCs by 0.3% during the period 2013-2021 (Ren et al., 2022). Despite these control strategies,

117 Southeast Asia experienced a rise in surface ozone levels. The prevalence of VOC-limited

118 photochemistry in this region led to reduced NOx titration, resulting in an ozone enhancement

119 (Souri et al., 2017; Lefohn et al., 2017). NOx or VOC are the major precursors that define the

120 ozone photochemical regimes when radiation levels are sufficiently high. The information of

121 ozone photochemical regimes is of utmost importance to control ozone pollution. However, the

122 non-linearity in the O_3-NOx-VOC chemistry has always posed a significant challenge in

123 identifying photochemical regimes. The regime is called NOx-limited if the ozone production is

124 directly related to change in NOx, with no impact from VOC perturbations. Whereas the region

125 where ozone production is regulated by the ambient availability of VOCs, it is called VOC-limited

126 (Sillman et al., 1990; Kleinman, 1994). The ratios such as $O_3/(NO_y-NO_x)$, HCHO/NO$_y$,

127 HCHO/NO_2, H_2O_2/HNO$_3$ are adopted to diagnose the ozone photochemical regimes (e.g., Sillman,

128 1995; Martin et al., 2004; Duncan et al., 2010). Among these, the most widely used indicator to

129 identify regimes is the Formaldehyde (HCHO) to Nitrogen dioxide (NO_2) Ratio (FNR) (Martin et

130 al., 2004; Duncan et al., 2010). In our study, we adopt FNR to identify NOx-limited or VOC-

131 limited regimes. On par with the current effort to mitigate ozone pollution, it is important to

132 understand how the changes in emissions of NOx and VOC affect the ozone photochemical

133 regimes and trends (Jin et al., 2017, 2020).

134

135 Ozone is the third strongest anthropogenic greenhouse gas forcer, also called a near-term

136 climate forcer (Myhre et al., 2013). The Intergovernmental Panel on Climate Change (IPCC) in

137 the fifth assessment report documented ozone changes in the troposphere during the industrial era

138   from 1750 to 2011 exerted a RF of 0.40 (0.20–0.60) $W.m^{-2}$ with a 5%–95 % confidence interval.

139   The increase in ozone during 1750–2011 has a global radiative forcing of $+0.35\ W.m^{-2}$ (Myhre et

140   al., 2013). The CMIP6 model from 1850 up to the present day estimated an ozone RF of

141     $0.39\ W.m^{-2}$ [0.27–0.51] (Skeie et al., 2020). The knowledge of ozone radiative forcing due to

142   changes in anthropogenic emissions of NOx and VOC will be helpful to assess climate change.

143   In this study, we also assess the impacts of enhanced or reduced emissions of NOx and VOC on

144   ozone radiative forcing in addition to ozone trends and photochemical regimes. To achieve this,

145   we conducted sensitivity experiments by doubling and halving global NOx and VOC emissions

146   using the state-of-the-art chemistry-climate model ECHAM6-HAMMOZ. The paper is outlined as

147   follows: satellite data and the model experimental setup are given in section 2, results are given in

148   section 3 that includes comparison of simulated tropospheric column ozone with satellite data and

149   estimated ozone trends. Discussions on ozone photochemical regimes and their trends are made in

150   section 4 and 5. Estimates of ozone radiative effects are given in section 6. Conclusions are made

151   in section 7.

152

153   **2.   Satellite data and model experiments**

154   **2.1. OMI Satellite Data**.

155

156   We include OMI/MLS tropospheric column ozone (TCO) for October 2004–December 2020 and

157   OMI NO_2, HCHO data for latitude range 60°S–60°N (**Ziemke et al., 2006**). OMI/MLS TCO Yis

158   determined by subtracting MLS stratospheric column ozone (SCO) from OMI TCO each day at

159   each grid point. Tropopause pressure used to determine the SCO invoked the WMO a $2\ K.km^{-1}$

160   lapse-rate definition from the NCEP reanalyses. The MLS data used to obtain SCO were derived

161 from the MLS v4.2 ozone profiles. We estimate 1σ precision for the OMI/MLS monthly-mean

162 gridded TCO product to be about 1.3 DU. Adjustments for drift calibration and other issues (e.g.

163 OMI row anomaly) affecting OMI/MLS TCO are discussed by Ziemke et al. (2019) and Gaudel

164 et al. (2024).

165 OMI NO_2 Monthly Mean Level 3 dataset consists of the monthly averaged tropospheric NO_2

166 column density as measured by the OMI from October 2004 to March 2021. The data were first

167 spatially averaged in a 1 by 1 degree grid, using a minimum spatial coverage threshold of 30% and

168 then temporally averaged (with a minimum temporal coverage of 10%). We have applied the

169 averaging kernel to model data for comparison with the model.

170

171 **2.2 IASI-SOFRID**

172 The Software for a Fast Retrieval of Infrared Atmospheric Sounding Interferometer (IASI) data

173 (SOFRID) retrieves global ozone profiles from IASI radiances (Barret et al., 2011, 2021). It is

174 based on the RTTOV (Radiative Transfer for TOVS) operational radiative transfer model jointly

175 developed by ECMWF, Meteo-France, UKMO and KNMI within the NWPSAF (Saunders et al.,

176 1999; Matricardi et al., 2004). The RTTOV regression coefficients are based on line-by-line

177 computations performed using the HITRAN2004 spectroscopic database (Rothman et al., 2005),

178 and the land surface emissivity is computed with the RTTOV UW-IRemis module (Borbas et al.,

179 2010). The IASI-SOFRID ozone for the study period (2008 to 2020) is obtained from METOP-A

180 (2008-2018) and METOP-B (2019-2020).

181

182   We use the SOFRID version 3.5 data presented and validated in **Barret et al. (2021)**, which uses

183   dynamical a priori profiles from an O_3 profile tropopause-based climatology according to

184   tropopause height, month, and latitude (Sofieva et al., 2014). The use of such an a priori has largely

185   improved the retrievals, especially in the southern hemisphere where the previous version was

186   significantly biased. The retrievals are performed for clear-sky conditions (cloud cover fraction <

187   20%). IASI-SOFRID ozone retrievals provide independent pieces of information in the

188   troposphere, the UTLS (300–150 hPa), and the stratosphere (150-25 hPa) (**Barret et al., 2021**).

189   SOFRID TCO absolute biases relative to ozonesondes are lower than 8 % with root mean square

190   error (RMSE) values lower than 18 % across the six 30° latitude bands (see Barret et al., 2021).

191   Importantly, Barret et al. (2021) have shown that relative to ozonesondes, TCO from IASI-

192   SOFRID display no significant drifts (<2.1 % decade^{-1}) for latitudes lower than 60°N and in the

193   SH for latitudes larger than 30° (<3.7 % decade^{-1}). But significant drifts are observed in the SH

194   tropics (-5.2% decade^{-1}) and in the NH at high latitudes (12.8% decade^{-1}). We have applied the

195   averaging kernel to model data for comparison with the model.

196

197

198   **2.3 IASI+GOME2**

199   IASI+GOME2 is a multispectral approach to retrieve the vertical profile of ozone and its

200   abundance in several partial columns. It is based on the synergy of IASI and GOME2 spectral

201   measurements in the thermal infrared and ultraviolet spectral regions, respectively, which are

202   jointly used to improve the sensitivity of the retrieval for the lowest tropospheric ozone (below 3

203   km above sea level, see **Cuesta et al., 2013**). Studies over Europe and East Asia have shown

204   particularly good capabilities for capturing near-surface ozone variability compared to surface in

205   situ ozone measurements (**Cuesta et al. 2018; 2022; Okamoto et al., 2023**). TCOs from

206   IASI+GOME2 also show good agreement with several datasets of in-situ measurements for a four-

207   year period in the tropics, with almost negligible biases and high correlations (**Gaudel et al., 2024**).

208   This ozone product provides global coverage for low cloud fraction conditions (below 30%) for

209   12 km diameter pixels spaced 25 km apart (at nadir). The IASI+GOME2 global dataset is publicly

210   available through the French AERIS data center, with data from 2017 to the present (available at

211   (O3 (IASI+GOME2) – IASI portal, 2024) and covers the 90° S-90° N latitude band. For this study,

212   we use the monthly TCO data between the surface and the tropopause for 2017 - 2022 for different

213   latitude bands. We have applied the averaging kernel to model data for comparison with the model.

214

215   **2.4 TROPOMI**

216   The TROPOspheric Monitoring Instrument (TROPOMI) is the sole payload on the Copernicus

217   Sentinel-5 Precursor (Sentinel-5P or S5P) satellite, which provides measurements of multiple

218   atmospheric trace species, including NO_2 and HCHO, at high spatial and temporal resolutions

219   (Veefkind et al., 2012). TROPOMI has a 108° field of view and spans the ultraviolet-visible (270–

220   495 nm), near-infrared (675–775 nm), and shortwave infrared (2305–2385 nm) wavelength ranges

221   at the nadir view. It has a daily global coverage with a spatial resolution of 5.5×3.5 km^2 at nadir

222   since a long-track pixel size reduction on 6 August 2019. We have used the Tropospheric column

223   of NO_2 and HCHO data for our study. We have applied the TROPOMI averaging kernel to model

224   data for comparison with the model.

a.   2.5 The ECHAM6-HAMMOZ model experiments

The ECHAM6.3-HAM2.3-MOZ1.0 aerosol chemistry–climate model (Schultz et al., 2018) used in the present study comprises the general circulation model ECHAM6 (Stevens et al., 2013), the tropospheric chemistry module, MOZ (Stevenson et al., 2006) and the aerosol module, Hamburg Aerosol Model (HAM) (Vignati et al., 2004). The gas phase chemistry is represented by the Jülich Atmospheric Mechanism (JAM) v002b mechanism (Schultz et al., 2018). This scheme is an update and an extension of terpenes and aromatics oxidation based on the MOZART-4 model (Emmons et al., 2010) chemical scheme. Tropospheric heterogeneous chemistry relevant to ozone is also included (Stadtler et al., 2018). MOZ uses the same chemical preprocessor as CAM-Chem (Lamarque et al., 2012) and WACCM (Kinnison et al., 2007) to generate a FORTRAN code containing the chemical solver for a specific chemical mechanism. Land surface processes are modeled with JSBACH (Reick et al., 2013). Biogeninc VOC emissions are modeled with the MEGAN algorithm (Guenther et al., 2012) which has been coupled to JSBACH (Henrot et al., 2017). The lightning NOx emissions are parameterized in the ECHAM6-HAMMOZ as per Rast et al. (2014). The lightning parameterization is the same in all the simulations. The model simulations were performed for the period 1998 to 2020 using Atmospheric Chemistry and Climate Model Intercomparison Project (ACCMIP) (Lamarque et al., 2010, van Vuuren et al., 2011) emission inventory. ACCMIP emission inventory includes emissions from agriculture and waste burning, forest and grassland fires, aircraft, domestic fuel use, energy generation, including fossil fuel extraction, industry, ship traffic, solvent use, transportation, and waste management. We used the high emission scenario Representative Concentration Pathway (RCP) 8.5 emissions (van Vuuren et al., 2011) to show their impact on ozone variability and trend.

247

248   The model is run at a T63 spectral resolution corresponding to about 1.8° × 1.8° in the horizontal

249   dimension and 47 vertical hybrid σ–p levels from the surface up to 0.001 hPa. The details of model

250   parameterizations and validation are described by Fadnavis et al. (2019a,b; 2021a,b; 2022, 2023).

251   We performed five experiments: (1) control and four emission sensitivity experiments: (2)

252   doubling anthropogenic emission of NO_X globally (DNOx), (3) reduce anthropogenic emissions

253   of NO_X by 50 % globally (HNOx), (4) doubling anthropogenic emissions of all VOCs globally

254   (DVOC), (5) reducing anthropogenic emissions of all VOCs by 50 % globally (HVOC). We

255   performed each experiment from 1998 to 2020 after a spin-up of one year. In each experiment, the

256   monthly varying AMIP-II Sea surface temperature and Sea ice representative of the period 1998–

257   2020 were specified as a lower boundary condition. VOCs considered in this study are listed in

258   the supplementary table-S1.

259

260   The tropospheric column ozone (TCO) is computed from the satellite data and model simulations

261   by averaging O_3 amounts from the surface up to the tropopausIe. Tropopause is as per WMO

262   thermal tropopause; the lowest level at which the temperature lapse rate decreases to 2 K.km^{-1} or

263   less (Maddox and Mullendore, 2018). For comparison of the model with satellite datasets, e.g.

264   IASI-SOFRID, OMI/MLS, we use model and satellite data for the same period, also, apply an

265   averaging kernel of each satellite on the model data during the respective comparison.

266   **2.5 Tropospheric ozone radiative effects**

267   The tropospheric ozone radiative effect (TO3RE) is calculated as in Pope et al (2024). While the

268   radiative forcing calculated in ECHAM6–HAMMOZ also includes impacts of aerosols and

269   dynamical effects, here we isolate TO3RE by using the Rap et al. (2015) tropospheric ozone

270   radiative kernel derived from the SOCRATES offline radiative transfer model (Edwards and

271   Slingo, 1996), including stratospheric temperature adjustments. To calculate the TO3RE, the

272   monthly averaged ECHAM6-HAMMOZ simulated ozone field is multiplied by the offline

273   radiative kernel (at every grid box). It is then summed from surface to the tropopause. The

274   simulated ozone data are mapped onto the spatial resolution of the radiative kernel and then

275   interpolated vertically onto its pressure grid. The equation for each grid box is

276   $TO3RE = \sum_{i=surf}^{trop} RK_i \times O_{3i} \times dp_i / 100$ (1)

277   where TO3RE is the tropospheric ozone radiative effect (W.m^{-2}), RK is the radiative kernel

278   (W.m^{-2}.ppbv^{-1}.100 hPa^{-1}), O_3 is the simulated ozone grid box value (ppbv), dp is the pressure

279   difference between vertical levels (hPa), and i is the grid box index between the surface pressure

280   level and the tropopause pressure. The tropopause pressure is based on the World Meteorological

281   Organization (WMO) definition of "the lowest level at which the temperature lapse rate decreases

282   to 2 K.km^{-1} or less" (WMO, 1957). Several past studies have used this approach of using the

283   SOCRATES offline radiative kernel with output from model simulations to derive the TO3RE

284   (Pope et al., 2014, Rap et al., 2015, Scott et al. 2018, and Rowlinson et al. 2020).

285   **3. Results**

3.1 Comparison of Latitudinal Variation Seasonal Cycle in TCO Satellites Retrievals

In this section, we compare the estimated TCO from the model (CTL) simulation with OMI/MLS (2006-2020), IASI-SOFRID (2008-2020), and IASI-GOME2 (2017-2020) satellite retrievals. We compared simulated TCO for the same period as individual satellite retrievals and applied an averaging kernel of that satellite to the model. The comparison of monthly mean TCO is made for 20° latitude bins in Figure 1. In the northern tropics (0°-20°N) (Fig 1a), the OMI/MLS data exhibits an annual cycle with a peak in April, whereas the model indicates a peak in January. Both datasets show a minimum in August. The model underestimates TCO by 1.8 to 4 ppb during March to October. In the 21-40 °N and 41-60 °N latitude bands (Fig. 1 b-c), the model shows a one-month lead in the peak of the annual cycle compared to OMI/MLS. Within these bands, the model underestimates OMI/MLS TCO by (2.8 - 6.1 ppb) during the summer months (May-August), while it overestimates TCO by 0.6 - 8.4 ppb during November to February. The 41-60 °N latitude band exhibits an overall underestimation (1.5 - 3.2 ppb) in June-July while it overestimates (0.7 - 5.9 ppb) rest of the year. In the Southern Hemisphere 9SH), OMI/MLS and the model show a similar pattern in the seasonal cycle. There is a consistent underestimation in the model for all months by 9 to 16.9 ppb in the 0-20 °S; 15.9 - 25.3 ppb in 21-40 °S and 41-60 °S. The comparison of TCO from IASI-SOFRID with the model shows features similar to those in the OMI/MLS. In the 0-20 °N latitude band, the model underestimates the TCO by about 3.6 to 7.5 ppb during April to October and in the 21-60 °N latitude band by 1.8 - 11 ppb in summer (May-August). In the SH, the model shows a closer association in TCO with IASI-SOFRID compared to OMI/MLS. During the SHc winter (June-August), the model overestimates TCO by 10 - 19.2 ppbv in the latitude range of 0-40 °S. Conversely, it underestimates TCO by 17.7 - 23.4 ppbv in the 41-60 °S

14

308 throughout the year, which is less compared to other satellite datasets. IASI-SOFRID is known to

309 suffer from negative drifts in the SH.

310

311 Interestingly, the model exhibits a fair agreement with IASI-GOME2 retrieved TCO during the

312 summer months (May-August) in the entire Northern Hemisphere (NH). During the winter

313 months, the estimated TCO shows a large overestimation of 8.3 - 11.7 ppb in the NH (0-40 °N).

314 In the SH, a fairly good agreement is observed between the model and IASI-GOME2 TCO,

315 especially in the 0-40 °S latitude band. The model overestimates the TCO by 7.4 - 8.8 ppb in the

316 0 - 20 °S during SH winter and underestimates by 4.7 - 6.7 ppb in the 21 - 40 °S band during SH

317 summer (December-January-February). An overall underestimation of about 7 - 11.2 ppb in TCO

318 is noted in the 41-60 °S throughout the year. Figure 1 shows that a peak in the seasonal cycle, in

319 the model is earlier than the three satellite data between 40°N and 40°S. In general, the model

320 underestimates TCO in summer in the NH and overestimates in winter relative to OMI-MLS, and

321 IASI-SOFRID. In the SH, the model underestimates TCO throughout the year compared to OMI-

322 MLS, IASI-SOFRID and IASI-GOME2. This underestimation is large for OMI/MLS, while IASI-

323 SOFRID and IASI-GOME2 are larger than the model in the latitude band 0-40 °S during the SH

324 winter. Although the model-satellite comparison is done for the same time period and averaging

325 kernel of each of the satellites are applied on the model during comparison, the differences in

326 sampling between the model and satellite measurements may cause these differences. It should be

327 noted that there are differences among the satellites. The resolution of each of the data (CTL

328 1.8°×1.8°), IASI-SOFRID (5°×5°), IASI-GOME2 (..), and OMI/MLS (5°×5°) is different. This

329 may be causing differences among them.

15
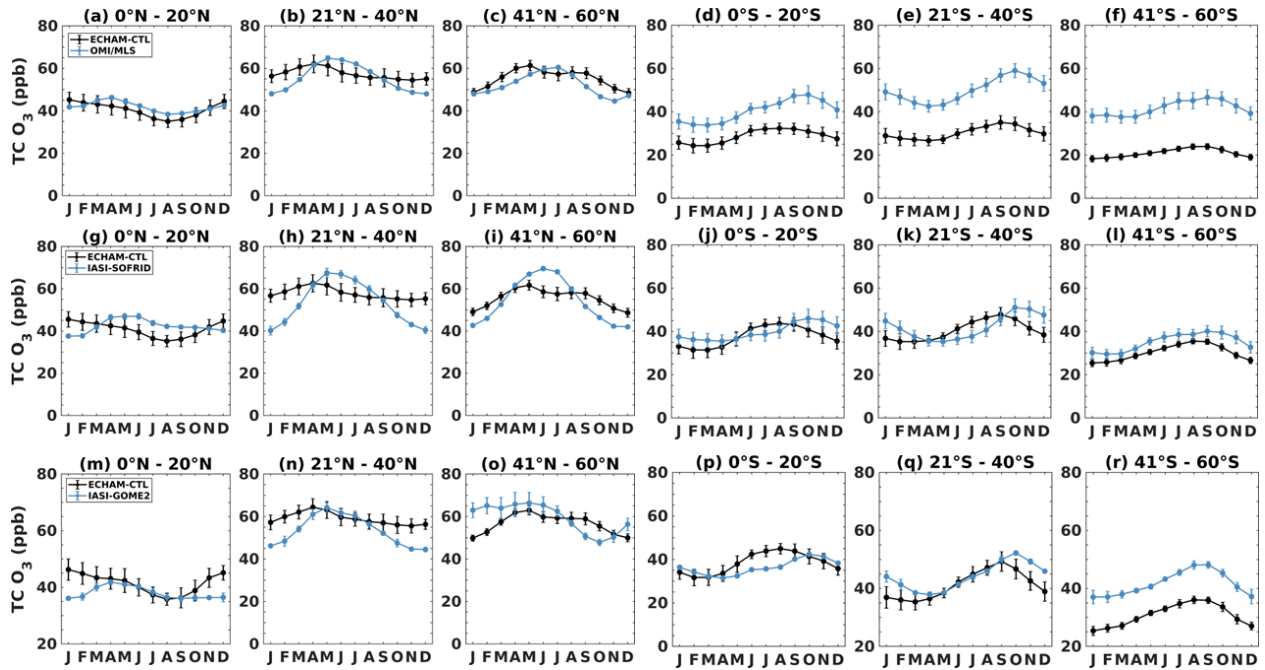
Figure 1: Monthly mean time series of TC ozone (ppb) averaged for 20° wide latitude bins from (a-f) OMI-/MLS (blue) and ECHAM6-HAMMOZ CTL simulations (black) for the time period October 2004-December 2020. (g-l) same as (a-f) but for IASI-SOFRID (blue) and ECHAM6-HAMMOZ CTL simulations (black) for the time period January 2008- December 2020, and (m-r) same as (a-f) but for IASI+GOME2 (blue) for time period January 2017 - December 2022 and ECHAM6-HAMMOZ CTL simulations (black) for the time period January 2017 - December 2020. The vertical bars in the figures represent 1σ standard deviation.

Further, we compare the simulated tropospheric column NO_2 and HCHO with the ESA CCI+ monthly averaged TROPOMI and OMI data (Glissenaar et al., 2024) (Fig. 2). The simulated NO_2 reproduces the seasonal cycle but overestimates in the NH and SH tropics in TROPOMI and OMI (Fig. 2 a-f) by 0.12 to 0.4 $\times 10^{15}$ molecules.cm^{-2} in the NH, and by 0.01 to 0.1 $\times 10^{15}$ molecules.cm^{-2} in the SH. Simulated NO_2 shows a underestimation in the 21-60°N latitude belts in the NH (0.8x10^{15} molecules.cm^{-2}) except in summer season and fairly good agreement in the SH 21-60°N (0.6 to 1.5×10^{15} molecules.cm^{-2}).

346   Simulated HCHO (Fig. 2 g-l) is overestimated in 0-20° N belt during January-February and July-

347   December (by 0.2-1 x 10^{15} molecules.cm^{-2}) compared to TROPOMI. However, it shows

348   underestimation compared to OMI by 2-3 x 10^{15} molecules.cm^{-2}. The simulated HCHO shows

349   underestimation over all the latitude bands except 0-20°N compared to TROPOMI and OMI. It

350   should be noted that TROPOMI/OMI monthly means are valid for clear-sky situations, whereas

351   the model simulations are 31-day all-sky averages. In previous studies (Boersma et al., 2016 and

352   references therein), it was shown that NO_2 is typically 15-20% lower on clear-sky days than under

353   cloudy situations due to lower photolysis rates, and slower chemical loss of NO_2. This effect likely

354   explains part of the model overestimate compared to TROPOMI NO_2. For HCHO the effect is

355   smaller because HCHO is both produced and destroyed by OH (see Fig. 4 in Boersma et al. 2016).

356   Considering these differences we proceed for the analysis of TCO trends, ozone photochemical

357   regimes, and ozone radiative effects. The overestimation/underestimation of ozone will be more

358   or less the same in CTL, DNOx, DVOC, HNOx and HVOC simulations. The anomalies DNOx -

359   CTL, DVOC - CTL, HNOx - CTL, and HVOC - CTL will be less impacted by the

360   overestimation/underestimation of TCO in the model.

361

17
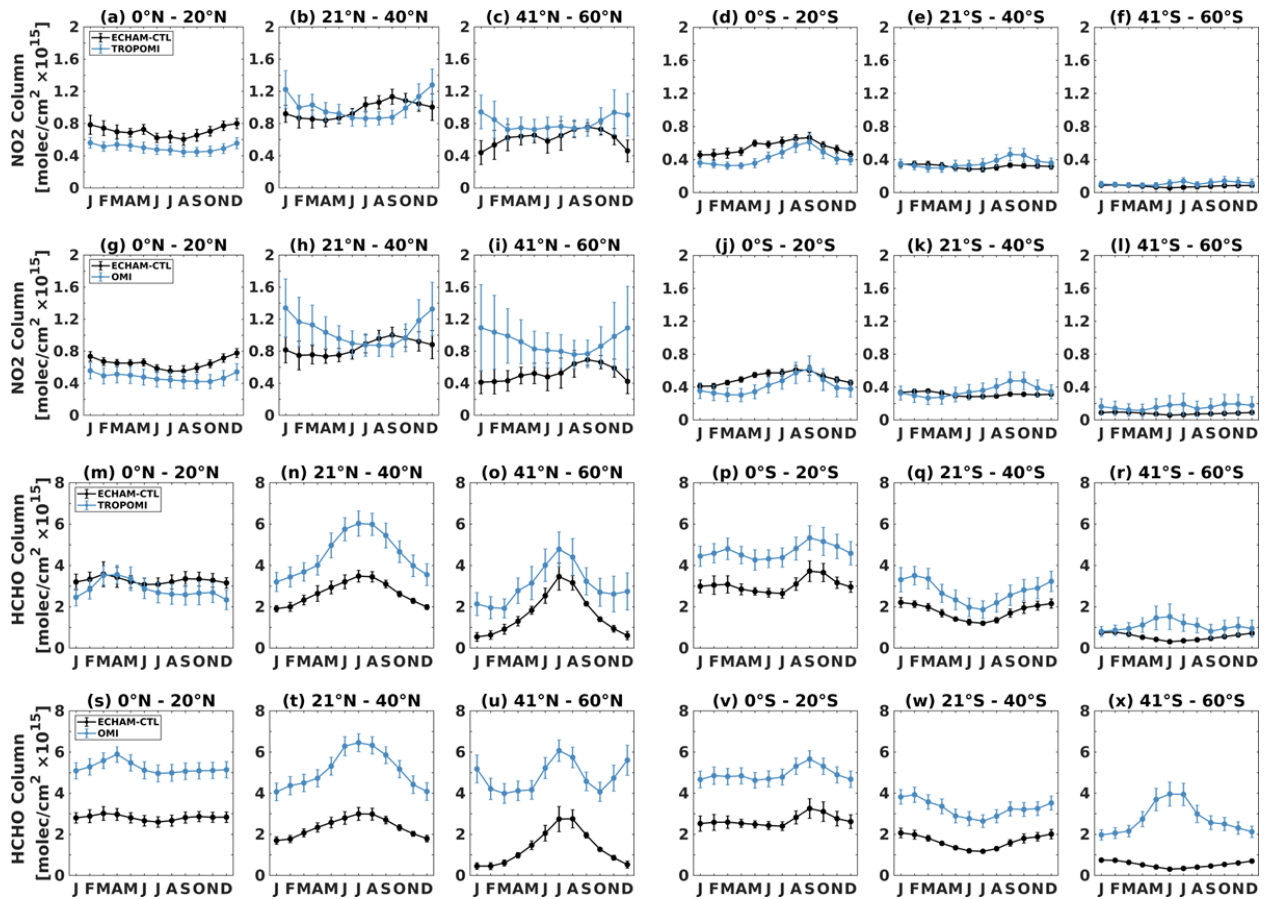
Figure 2: Monthly mean time series of TC NO_2 (ppb) averaged for 20° wide latitude bins from ECHAM6-HAMMOZ CTL simulations (black) for the time period same as TROPOMI satellite for (a-f) (May 2018 - December 2020), (g-l) same as a-f but for HCHO. The vertical bars in the figures represent 1σ standard deviation. The 1σ standard deviation is estimated from data within the latitudinal belt during the period of observations.

3.2. Impacts of emission changes on the spatial distribution of ozone

Figure 3 shows the spatial distribution of the simulated surface (Fig. 3a-e) and tropospheric column ozone (TCO) (Fig. 3f-j) concentration from ECHAM-CTL simulations and the differences in DNOx - CTL, DVOC - CTL, HNOx - CTL, and HVOC - CTL simulations for the period 1998-

18

375   2020. The CTL simulation shows high surface ozone levels (19 - 61.1 ppb) between 10-40 °N (Fig.

376   3a). Doubling of NOx emission (DNOx) causes a global mean enhancement of surface ozone by

377   4.1 ppb. Surface ozone increases by 5-20 ppb compared to the control scenario across most of the

378   globe, excluding highly urbanized regions like the Indo-Gangetic plains (IGP), Southeast China,

379   Northeastern US, and Europe. (Fig. 3b). Over these regions, a large reduction (8 to 20 ppb) in

380   surface ozone is noticed in response to DNOx conditions indicating ozone titration by NO_X. While

381   an increase in surface ozone concentrations is observed globally for DVOC (0.92 ppb), its

382   magnitude is less than that of the DNOx condition (Fig. 3c). The largest increase in surface ozone

383   concentration for DVOC is observed over Indo-Gangetic Plains, Eastern China and the Eastern

384   United States (3-6 ppb). Interestingly, these are the same regions where a decrease in ozone is

385   observed in the DNOx simulation. The decrease (increase) in ozone with an increase in NOx

386   (VOC) indicates that these regions could be NOx-saturated or VOC-limited. Reduction of NO_X

387   emissions (HNOx-CTL) simulations show a reduction in surface ozone globally (-2.53 ppb) except

388   over North-Eastern China (Fig. 3d). Earlier, Souri et al. (2017) reported that eastern Asia has

389   witnessed a rise in surface ozone levels despite NOx control strategies, indicating the prevalence

390   of VOC-limited photochemistry over this region (details in section 4 and 5). However, the absence

391   of such an increase over other VOC-limited regions points towards the possibility of nonlinear

392   ozone chemistry. While HVOC stimulation causes a reduction in surface ozone globally (-0.44

393   ppb), an increase is observed in South America, some parts of the US, Australia, and the Indo-

394   China peninsula (Fig. 3e). This increase could be due to a reduction in the radical destruction of

395   ozone caused by aromatic hydrocarbons in low NOx conditions observed in HVOC simulations

396   compared to CTL simulations in these regions (Taraborrelli et al., 2021).

397   On the other hand, the estimated global mean TCO from the ECHAM-CTL simulation

398   from 1998 to 2020 is 39.45 ppb. CTL simulations show higher amounts of TCO in the Northern

399   Hemisphere (NH) within the latitudinal band of 20° to 40°N (40.9 to 68.8 ppb). These

400   concentrations are pronounced over South and East Asia, spanning from the Mediterranean region

401   to eastern China (Fig. 3f). Doubling of anthropogenic NO_X emissions (DNOx) enhances the global

402   TCO by 11.7 ppb compared to CTL (Fig. 3g). The ozone enhancement exceeds the CTL by 6.1 -

403   29.3 ppb between 20°- 40°N, particularly over South Asia. Interestingly, in highly urbanized areas

404   such as the Indo-Gangetic plains, South-East China, Northeast US, and Europe, there is only a

405   marginal increase in ozone levels (~5 ppb). This suggests the existence of a distinct ozone

406   photochemical regime in these regions. Further exploration of this aspect will be conducted in

407   sections 4 and 5.

408   The impact of the doubling of VOC emissions (DVOC-CTL) on ozone is depicted in Figure 3h.

409   An increase in global mean TCO by 1 ppb is observed in this emission scenario. The spatial

410   distribution of TCO anomalies shows that enhancement in TCO is ten times less than that of

411   doubling NO_X condition (-0.8 - 3.6 ppb in DVOC compared to 5.6 - 29.3 ppb in DNOx) (Fig. 3g

412   and 3h). Large values of TCO (1.5-2) are observed in the high latitudes (north of 60°N) and South

413   and East Asia, with the largest values of more than 2.5 ppb over east China (e.g., Beijing).

414   Interestingly, in the tropical regions slight decreases in TCO are simulated. This is consistent with

415   the recent finding that aromatics, especially benzene, can lead to efficient ozone destruction in the

416   tropical UTLS (Rosanka et al., 2021). The TCO anomalies in response to the reduction of NO_X

417   emission by 50% (HNOx-CTL) show negative TCO anomalies all over the globe (Fig. 3i). The

418   global mean TCO is reduced by -3.73 ppb. Large decreases in TCO are observed over Arabia,

419   South and East Asian regions (2.6 - 12.8 ppb). Reducing VOCs by 50 % (HVOC) causes an overall

420   decrease in TCO of 0.27 ppb (Fig. 3j). A small enhancement is noted in the TCO by 0.5 - 1 ppb in

421   the southern tropics and South polar region, while a decrease of -2.3 to 0.3 ppb is observed in the

422   Northern Hemisphere. (Fig. 3j). Figure 3 clearly portrays that the TCO response to NOx emission

423   change is larger than that of VOCs and shows a spatially distinct distribution associated with the

424   region-specific ozone photochemical regimes (more discussion on the ozone photochemical

425   regimes will be detailed in section 4 and 5).
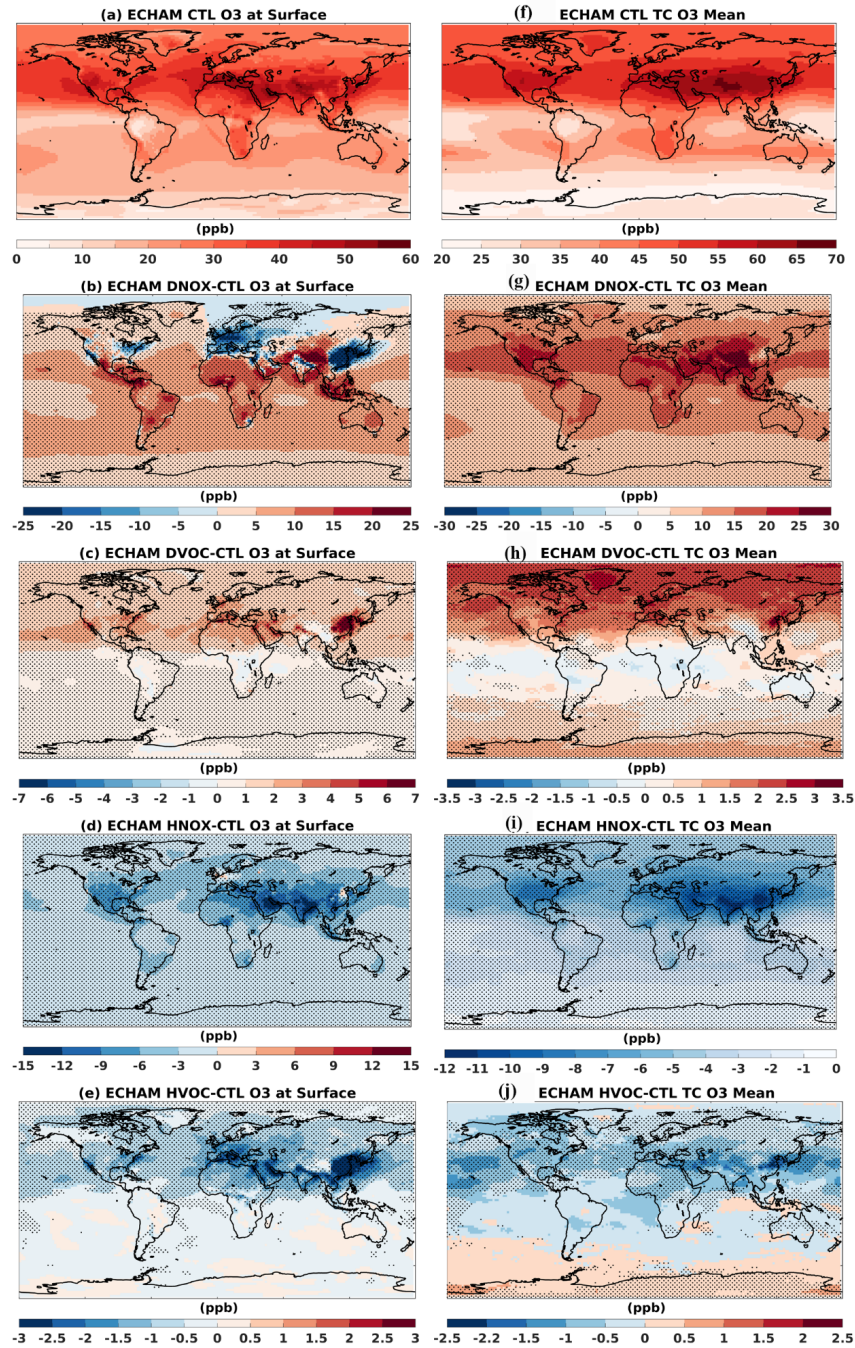
Figure 3: Spatial distribution of surface ozone (ppb) for (a) from CTL, (b) anomalies from DNOx - CTL, (c) anomalies from DVOC - CTL, (d) anomalies from HNOx - CTL, (e) anomalies from HVOC - CTL. Figures (f) to (j) are the same as those of figures (a) to (e) but for TCO. The stippled regions in the figures indicate anomalies significant at 95% confidence. The tropopause considered is WMO-defined lapse rate tropopause (WMO, 1957).

3.3. Spatial distribution of trends in TCO, NO₂ and HCHO

The trends in TCO estimated from ECHAM-CTL simulations are compared with satellite-retrieved TCO to gain more confidence in the model-derived trends. Since IASI-GOME2 has a short observation period and IASI-SOFRID has negative drift in the southern hemisphere, only OMI/MLS (October 2004 to December 2020) is considered for trend estimation and is shown in Figure 4. The spatial pattern of trends from OMI/MLS closely aligns with model simulations for the period October 2004 to December 2020. OMI/MLS show a slightly lower trend of 1.41 [-2.1; 4.5] ppb.decade^{-1} than model simulation 1.28 [-1.5;3.7] ppb.decade^{-1}. Both datasets reveal pronounced trends, ranging from 3-4 ppb.decade^{-1}, across regions such as South Asia, East Asia, the western Pacific, and the Southern Hemisphere between 0°-30°S. OMI/MLS show negative trends over parts of Africa, South America, Australia and the South-eastern Pacific (Fig. 4b), which is not simulated in ECHAM6-HAMMOZ. This may be due to the model's tendency to underestimate ozone levels and disparities in the seasonal cycle compared to OMI/MLS data. (see Fig. 1).

The CESM2-WACCM6 simulation from 1950 to 2014 also shows the largest estimated trends at 20–30° N of 0.8 Tg.decade^{-1} **(Fiore et al 2022)**. Recently, **Wang et al (2021)** reported TCO trends varying between 2.55 to 5.53 ppb.decade^{-1} during 1955-2017 over South and East Asia using IAGOS, ozonesonde observations, and GEOS-Chem simulations. Further, a large positive trend of ~2.5 ppb.decade^{-1} observed near 50°S in OMI/MLS is not simulated by the model (Fig. 4a-b). TCO trends analyzed from the Total Ozone Mapping Spectrometer (TOMS) indicate a consistent absence of trend over the tropical Pacific Ocean, with notable positive trends (5–9% per.decade^{-1})

453   seen in the mid-latitude Pacific regions of both hemispheres. This pattern is consistent across the

454   ECHAM6-HAMMOZ and OMI/MLS data, although their magnitude differs (Fig. 4 a-b). TOMS

455   data also showed trends of ~2–9% decade^{-1} across broad regions of the tropical South Atlantic,

456   India, Southeast Asia, Indonesia, and the tropical/subtropical regions downwind of China during

457   1979–2003 (Ziemke et al., 2005, Beig and Singh 2007).
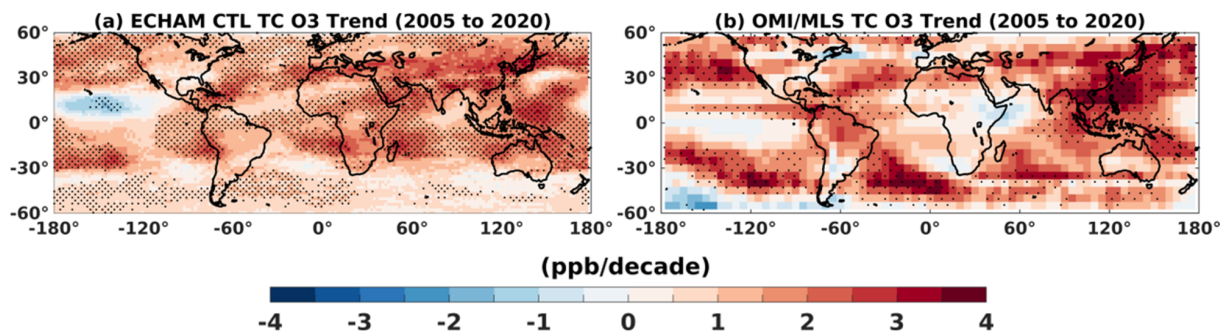
458

459   Figure 4: Trend of tropospheric column Ozone (TCO) (ppb/decade) from (a) ECHAM
460   CTL, and (b) OMI/MLS satellite for the period January 2005 to December 2020. Stippled regions
461   in the figures indicate trends significant at 95% confidence. The tropopause considered is WMO
462   defined lapse rate tropopause.

463

464   Figure 5 shows the spatial distribution of estimated trends in surface ozone and TCO from

465   ECHAM simulation for the period 1998-2020 from CTL, DNOx - CTL, DVOC-CTL, HNOx-

466   CTL, and HVOC - CTL. The surface ozone trend in the CTL simulation shows a pronounced

467   global increase, particularly notable over South Asia and the Middle East (Fig. 5a). This rise is

468   also seen in the TCO trend (Fig. 5f). However, the negative trends in surface ozone over Mexico,

469   certain parts of the US, and East China are barely discernible in the TCO data. This discrepancy

470   may stem from the interplay of mixing and transport processes, which are crucial when assessing

471   ozone levels across the total column. For a double-NOx emission condition, both surface ozone

24

472   and TCO exhibit large negative trends over India, China and Australia (-0.4 to -2 ppb.decade^{-1}),

473   while trends are positive over Europe, the US, some parts of Africa and South America (Fig. 5b

474   and 5g). A global mean increase in TCO trend by 1.2 [-5.3; 5.8] ppb.decade^{-1} is seen in a DNOx

475   simulation. Interestingly, a positive trend in TCO is seen over the oceanic regions downwind of

476   major continental regions like Africa, China and the US, which was absent in the surface ozone

477   trend, indicating the potential contribution of transport in the TCO trend (Fig. 5g). When global

478   emissions of VOCs are doubled, a decreasing trend (-0.8 to -1.9 ppb.decade^{-1}) in surface ozone is

479   noted over Europe, Africa and some parts of the US, while strong positive trends (1.6 to 2

480   ppb.decade^{-1}) are seen over India and China (Fig. 5c). Though the surface trends are faintly

481   captured in the TCO trend, an enhancement over South Asia, China, parts of the Indian Ocean,

482   and the western Pacific are noted (Fig. 5h). Compared to DNOx, the enhancement in the TCO

483   trend for DVOC is only marginal but shows a global mean trend of 0.5 [-0.85;1.93] ppb.decade^{-1}.

484   Reducing NO$_X$ and VOC emissions by 50% (HNOx and HVOC) decreases the global mean TCO

485   trends by 0.38 [-1.96;1.64] ppb.decade^{-1} and 0.42 [-0.96;1.61] ppb.decade^{-1} respectively. Though

486   a large positive trend is observed in some parts of China, India, US for both HNOx and HVOC

487   simulations, it is not that evident in their TCO trend.

488
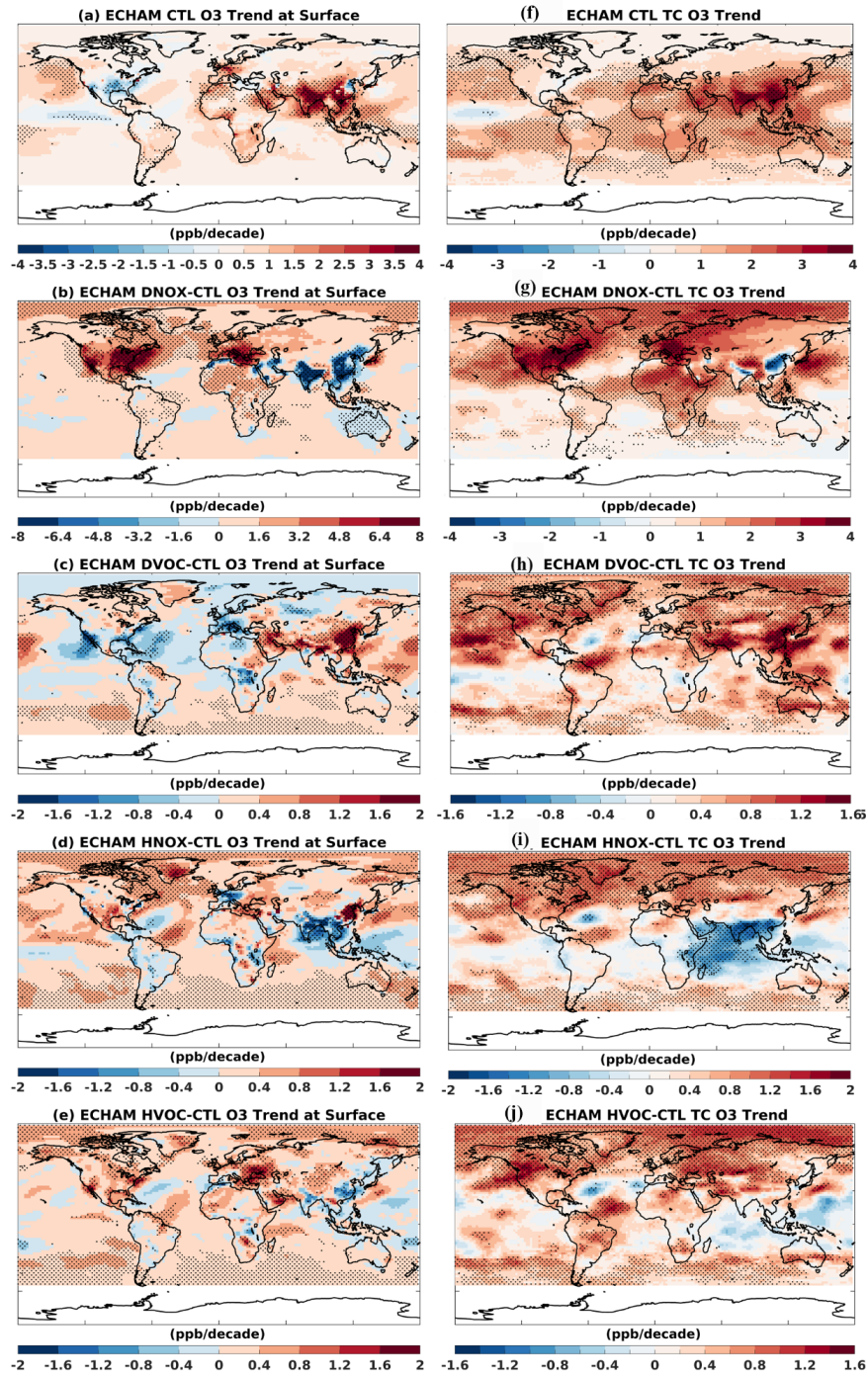
Figure 5: (a) Trend of surface ozone (ppb.decade^{-1}) from (a) CTL, (b) DNOx, (c) DVOC, (d) HNOx, (e) HVOC simulation. (f) to (j), same as that of figures (a)-(e) but for the tropospheric column ozone (TCO) trend. The stippled regions in the figures indicate significance at 95% confidence. The tropopause considered is WMO defined lapse rate tropopause.

3.4. Trends in emission and tropospheric column of NO₂ and HCHO

494   We show mean emissions of NOx and HCHO over urban/semi-urban regions; US, Brazil, Europe,

495   Africa, India, China, Australia in Figure 6. Figure 6 clearly portrays high emissions of VOCs and

496   NOx in India and China. Furthermore, VOCs emissions are noted to be higher than NOx over all

497   the regions. They are higher by a factor of 3.3 in the US, 11.3 in Brazil, 4.8 in Europe, 10.5 in

498   Africa,   10.8   in   India,   6.1   in   China,   and   6.7   in   Australia.

499
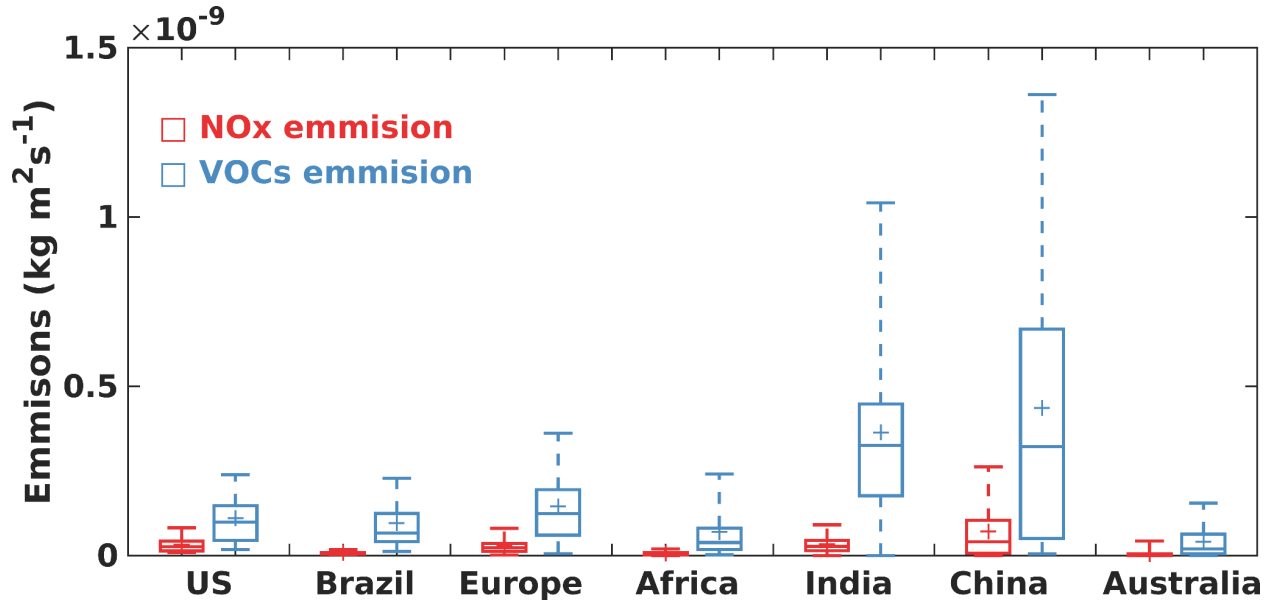
500   Fig. 6: Box and whisker plot illustrating the NOx and VOCs emission over the regions US (85°W

501   - 110°W, 35°N - 44°N), Brazil (34°W- 49°W, 24°S - 3°S), European Union (9°W - 45°E, 35°N -

502   55°N), Central Africa (14°W - 45°E, 0° - 14°N), India (75°E - 90°E, 8°N - 30°N), China (110°E -

503   125°E, 30°N - 42°N), South Australia (134°E - 154°E, 38°S - 28°S). The box represents the 25 and

504   75 percentile, and the whisker represents the 5 and 95 percentile. The plus marker represents the

505   mean and the horizontal bar represents the 1 and 99 percentile.

506   The trends in ozone are partly modulated by the change in the emission of its precursors

507   and partly by meteorology (e.g., Verstraeten et al., 2015). Further, we show trends in emissions

508   and tropospheric column amounts of ozone precursors NO₂ and HCHO, from ECHAM-CTL and

509   OMI satellite retrievals in Figure 7. NO₂ and HCHO are considered here because column

510 concentration of these will be used to identify the ozone photochemical regimes discussed later in

511 Sections 4-5. Emission and tropospheric columns of HCHO and NO_2 from ECHAM-CTL show

512 large positive trends over the South and East Asian regions (Figure 7a-d). These regions show

513 large positive ozone trends in both model and OMI satellite data (see Figures 4a-b and 5a,f). Over

514 Europe and the US, the emission trend in both HCHO and NO_2 is negative. Though a similar

515 negative trend in tropospheric column NO_2 is seen over these regions, a marginal positive trend

516 (insignificant) is noted for HCHO (Figures 7c-d). The positive trend in column HCHO could be

517 due to secondary production pathways from biogenic emissions or methane oxidation and transport

518 (e.g., Alvarado et al., 2020; Anderson et al., 2017). The positive trend in ozone (Figures 4a-b and

519 5a,f) along with a negative trend in NO_2 and HCHO (Figure 7a-d) over Europe indicates that ozone

520 production over this region has been initially controlled by VOCs (i.e., VOC-limited regime;

521 detailed discussed in section 4). However, a large decreasing trend in NO_2 compared to that of

522 HCHO over this region might have decreased the NOx titration effect, resulting in an increase in

523 ozone. On the contrary, a negative trend in surface ozone (Figure 5a) along with negative trends

524 in NO_2 and HCHO are seen over the US (Figure 7a-b). The decrease in both NO_2 and HCHO

525 would have resulted in a decreasing trend in surface ozone over this region. This also indicates

526 that the US might have been in a NOx-sensitive regime before and the large negative trend in NO_2

527 might have resulted in the decreasing trend in ozone (discussed further in section 4).

528

529 Further we compared the simulated trends in column HCHO and NO_2 with the OMI retrievals for

530 the period 2005-2020 (Figures 7e-h). OMI shows a positive trend in tropospheric column HCHO

531 over South Asia, parts of eastern China, the Iranian Plateau, the Amazon and central Africa. The

28

532   model simulated trends show reasonable agreement with OMI, except for some areas in central

533   Africa. Additionally, differences are seen in regions such as the US, Northern Africa, Australia,

534   and Argentina, where OMI indicates a negative trend, while the model suggests a marginal positive

535   trend. Both OMI and ECHAM CTL show a good agreement in the tropospheric column NO_2 trend.

536   Both datasets show negative trends over the US and Europe, and positive trends over the Middle

537   East, South Asia, and Eastern China. Thus, Figures 4, 5, and 7 clearly indicate the impact of ozone

538   precursors on the spatial distribution of ozone trends. Figure 7 further indicates the prevalence of

539   different ozone photochemical regimes associated with the availability of HCHO and NO_2. This

540   warrants a detailed discussion on the spatial distribution of ozone precursors and their impact on

541   ozone production sensitive regimes, which will be presented in the next section.
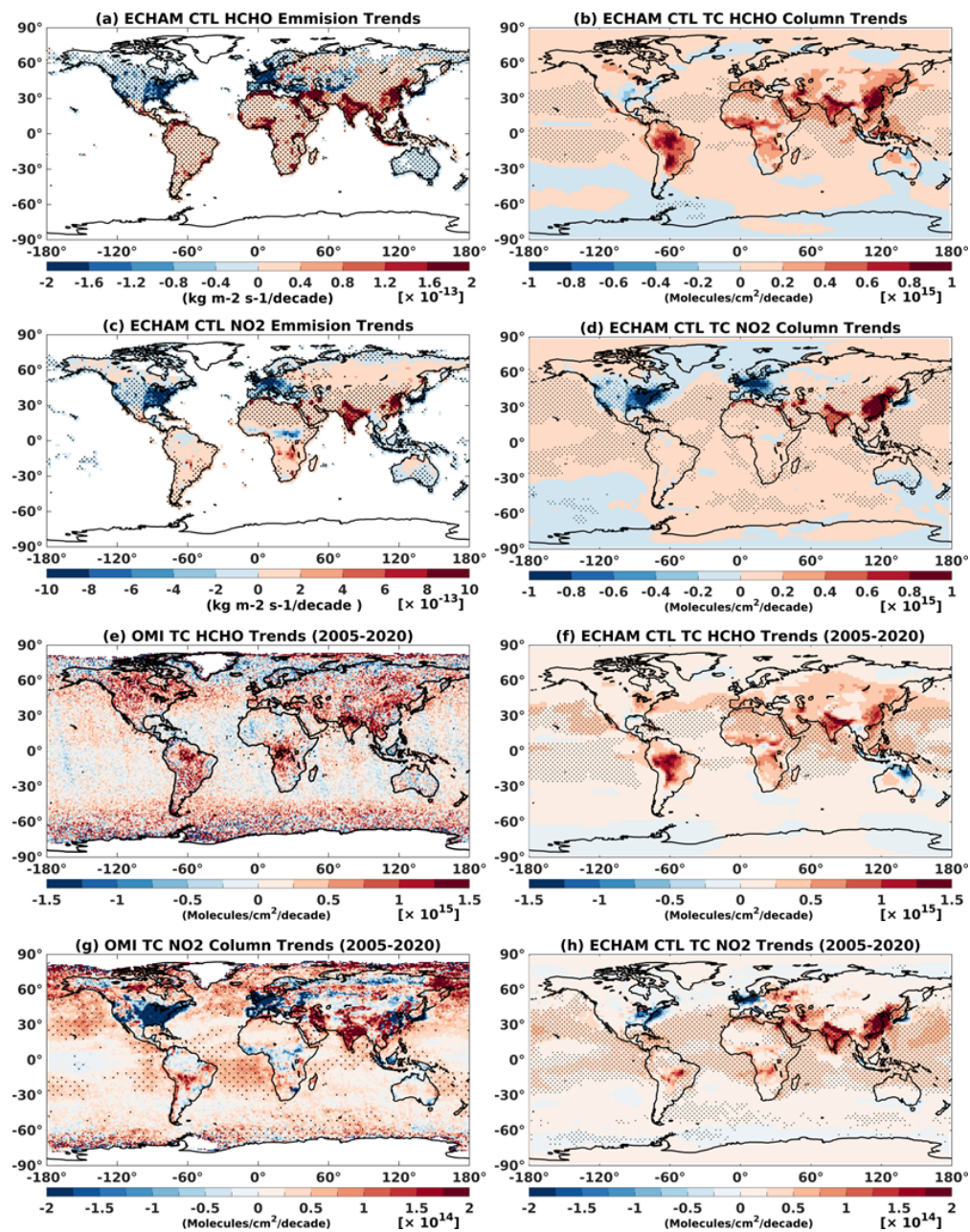
Figure 7: Trend in (a) anthropogenic emission of HCHO (kg.m^2.s^{-1}.decade^{-1}) (b) anthropogenic emission of NO$_2$ (kg.m^2.s^{-1}.decade^{-1}) (c) tropospheric column HCHO (molecules.cm^{-2}.decade^{-1}), and (d) tropospheric column NO$_2$ (molecules.cm^{-2}.decade^{-1}) from ECHAM CTL simulation for the period 1998-2020. (e) and (f) Trend in tropospheric column HCHO from OMI and ECHAM CTL simulation respectively for the period 2005-2020. (g) and (h) is the same as that of (e) and (f) but for tropospheric column NO$_2$. The stippled regions in the figures indicate data significance at 95% confidence. The tropopause considered for column estimate is WMO defined lapse rate tropopause.

30

551 **3. Influence of NOx and VOCs emissions on Formaldehyde to Nitrogen dioxide Ratio**

552 In this section, we diagnosed the spatial distribution of ozone production sensitivity regimes (NOx-

553 limited/VOC-limited) associated with different simulations of emission changes by using

554 formaldehyde to nitrogen dioxide ratio (FNR). We estimate the FNR thresholds from ECHAM6-

555 HAMMOZ model simulations adhering to the methodology outlined by Jin et al. (2017). The

556 method to obtain FNR involves two steps: (1) obtaining the ozone response from emission

557 sensitivity simulations (here, HNOx and HVOC simulations) and plotting it as a function of FNR

558 (Fig. 8a), (2) calculating cumulative probability from this data for the conditions $d[O_3]/dE_{NOx} < 0$

559 (NOx limited) and ($d[O_3]/dE_{NOx} > d[O_3]/dE_{VOC} > 0$) (VOC-limited) (Fig. 8b). This approach is

560 applied to estimate FNR thresholds to distinctly delineate the various ozone photochemical

561 regimes as NOx or VOC-limited over major urban and semi-urban regions over the globe. The

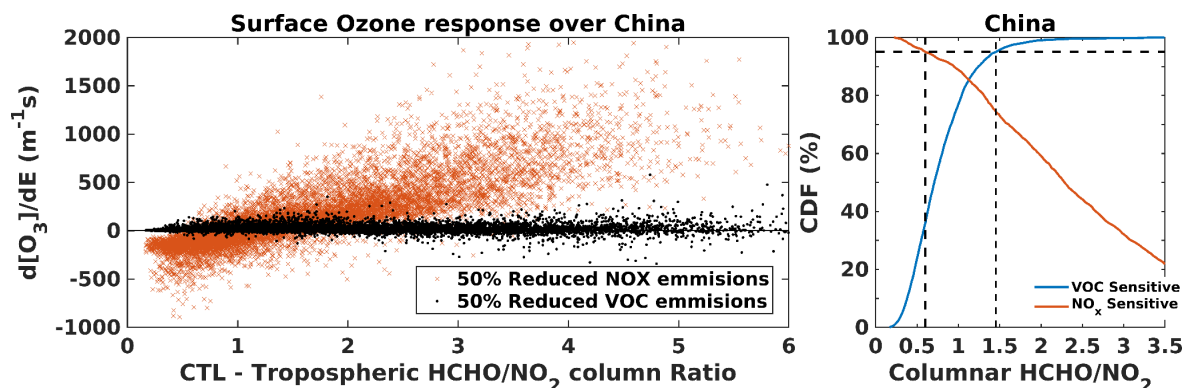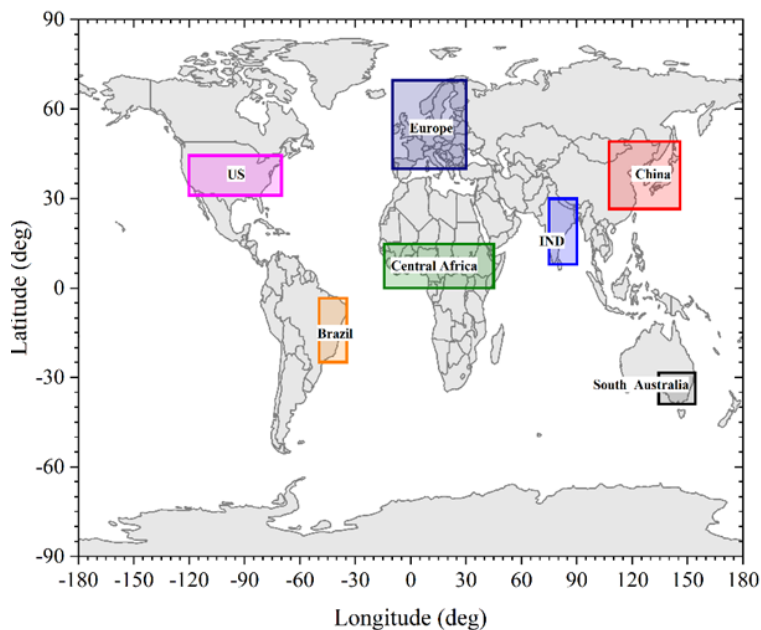562 regions considered for estimating the FNR are shown in Figure 9.

563
564 Figure 8: (a) Typical example of a normalized surface ozone sensitivity to a 50% reduction in
565 global NOx (HNOx) and VOC (HVOC) emissions versus tropospheric column HCHO/NO$_2$ ratio
566 derived from ECHAM6-HAMMOZ model simulation over China for the period 1998-2020 (b)
567 Cumulative probability (CP) of VOC-sensitive ($d[O_3]/dE_{NOx} < 0$) and NOx-sensitive ($d[O_3]/dE_{NOx}$
568 $> d[O_3]/dE_{VOC} > 0$) conditions, as a function of tropospheric column HCHO/NO$_2$ as simulated by
569 the ECHAM6-HAMMOZ model. The horizontal dashed line represents the 95% CP, and the
570 vertical dashed lines represent the HCHO/NO$_2$ ratio corresponding to 95% CP for both the VOC-
571 sensitive and NOx-sensitive curve demarcating the VOC-sensitive, NOx-sensitive, and transition
572 regimes.

31

573

Figure 9: The rectangular box marks indicate the regions considered for estimating the HCHO/NO$_2$ ratio (FNR).

Table 3 presents FNR thresholds across the regions outlined in Figure 8. Based on ECHAM6-HAMMOZ simulations, our analysis closely mirrors the threshold ranges documented in prior research. For instance, during summer in the USA, many studies report FNR thresholds within the 0.8-2 range (Roberts et al., 2022; Chang et al., 2016; Jin et al., 2017), while our simulations indicate a range of 0.3 to 1.05. Similarly, across China, previous studies (e.g., Lee et al., 2022; Chen et al., 2023) have reported FNR thresholds spanning 1-2/0.6-3, aligning closely with our simulated range of 0.6-1.45. It is interesting to note that the transition region exhibits a very narrower range in the US, Europe, and China, indicating that the transition from VOC-limited to NOx-limited can happen suddenly in response to changes in the emission of NOx/VOC. Whereas the transition region is wider in Central Africa.

587　Table 3. Estimated values of the tropospheric HCHO/NO$_2$ columns threshold ratios from
588　ECHAM6-HAMMOZ model control simulation to identify the NOx and VOC sensitive regimes
589　across various regions. The FNR less than the lower limit indicates VOC-limited, and that higher
590　than the upper limit indicates NOx-limited regimes.

591

Sr. No.	Regions	Transition limits	
1	US (85°W - 110°W, 35°N - 44°N)	0.44	1.14
2	Brazil (34°W- 49°W, 24°S - 3°S)	3.04	7.53
3	European Union (9°W - 45°E, 35°N - 55°N)	0.3	1.37
4	Central Africa (14°W - 45°E, 0° - 14°N)	3.24	7.19
5	India (75°E - 90°E, 8°N - 30°N)	2.27	4.63
6	China (110°E - 125°E, 30°N - 42°N)	1.14	1.91
7	South Australia (134°E - 154°E, 38°S - 28°S)	1.03	3.28

592
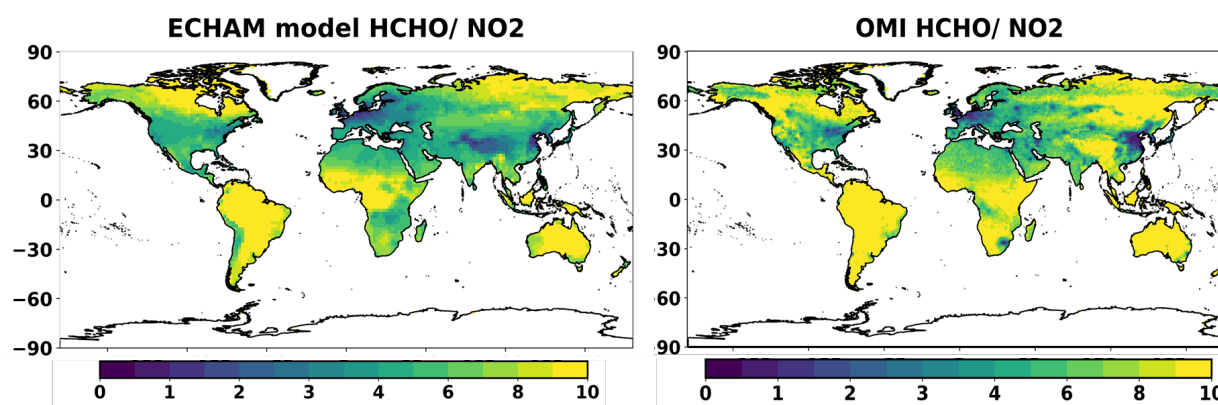
593

594　Figure 10: Spatial distribution of mean tropospheric column HCHO/NO$_2$ (FNR) obtained from
595　ECHAM6-HAMMOZ CTL simulations (2005-2020) and OMI (2005-2020).

596

597　To enhance our confidence in the model estimations, we compared the model-estimated FNR with

598　the OMI-derived FNR for the period 2005-2020. Figure 10 illustrates the comparison of FNR

599   estimated from ECHAM6-HAMMOZ CTL simulations with OMI. The spatial map of FNR shows

600   fairly good agreement between OMI and the model. Over the urbanized regions (e.g., South Asia,

601   Europe, the US, and China) both the model and OMI show FNR < 4. In contrast, regions like North

602   Canada, South America, central Africa, Australia, and Siberia exhibit high FNR values >9.

603   Although there is good agreement of the model simulations with OMI, some minor differences are

604   seen between the model and OMI FNR over the west coast of South America, South Africa, the

605   Tibetan Plateau, and western Australia. These differences could be due to the underestimation of

606   HCHO in the model over these regions. Considering the fair performance of the model in

607   comparison with OMI, we further analyzed the influence of NOx and VOC emissions on the FNR

608   based on the model simulations, which are discussed in the subsequent sections.

609   Fig. 11 shows the spatial distribution of estimates of FNRs from CTL, DNOx, DVOC,

610   HNOx, and HVOC simulations. In the control simulation for the period 1998-2020, most of the

611   polluted cities/industrialized areas in the US, Canada, Europe, west Russia, East China, Korea and

612   Japan are VOC limited (FNRs <2). The NOx-limited regimes (largest FNR values >5) are found

613   over the tropical rainforest, savanna, and arid climates clearly reflect the rural or unpolluted

614   background regions where large biogenic emissions of VOCs are high (e.g., Shen et al., 2019;

615   Millet et al., 2008) (see Table 3 and central Africa in Fig. 10f). The DNOx simulation yields a

616   significant shift in the spatial extent of VOC-limited regimes (Fig. 10bS). Regions across the NH

617   exhibit VOC-limited regimes, except central Africa, Amazonia, and north Australia. Notably, the

618   SH exhibits minimal change in the spatial extent of VOC-limited regimes with consistent

619   occurrences over the western coastlines of South America, Argentina, Brazil, South Africa, and

620   southern Australia.

621   The DVOC simulations show (Fig. 11c) a persistent occurrence of VOC-limited regimes over

622   Western Europe (e.g., the UK). The moderate FNR values (1-6) prevail across most of the NH,

623   indicating a transition or NOx-limited regime. The spatial distribution of FNR in the SH is similar

624   to that of the control simulation. In Figure 3b-c, the increase in ozone in response to a decrease in

625   NOx and an increase in VOC is attributed to the existence of a VOC-limited regime over these

626   regions. The Indo-Gangetic Plains, Eastern China and the eastern United States clearly indicate

627   the VOC-limited condition. The comparison of CTL and HNOx simulation (Fig. 10d) shows the

628   transition from VOC-limited regimes to NOx-limited regimes occurring globally.

629   The FNR distribution for HVOC simulations is similar to CTL (as depicted in Fig. 10e) without

630   any notable change in the spatial pattern. This suggests that ozone photochemistry exhibits less

631   sensitivity to halved VOC emissions. Figure 11 clearly depicts that DNOx and HNOx simulations

632   greatly impact the shift in ozone photochemical regimes compared with DVOC and HVOC

633   simulations. This indicates that ozone photochemistry is highly sensitive to changes in NOx

634   emissions globally.

35
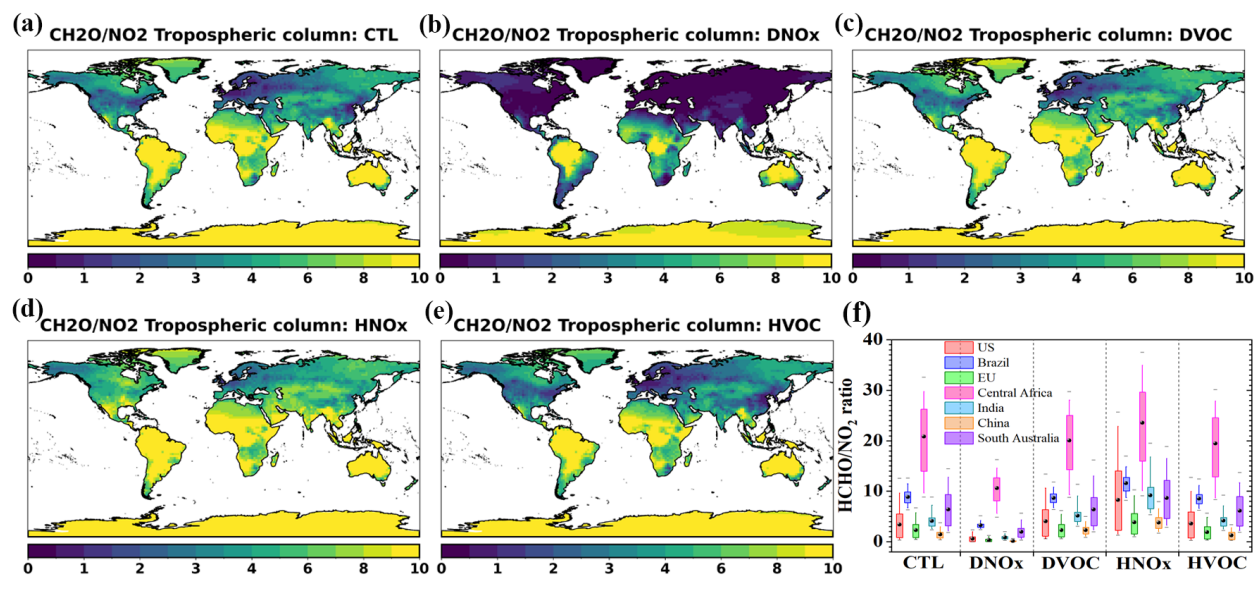
Figure 11: Spatial distribution of monthly mean tropospheric column HCHO/NO$_2$ (FNR) obtained from ECHAM6-HAMMOZ simulations (1998-2020) for (a) CTL, (b) DNOx, (c) DVOC, (d) HNOx, and (e) HVOC simulations. (f) Box and whisker plot illustrating the long-term average FNR over the regions depicted in Fig.7. Box represents 25 and 75 percentile and whisker represents 5 and 95 percentile. The black spherical marker represents the mean and the horizontal bar represents the 1 and 99 percentile.

5. **Seasonal variation of Formaldehyde to Nitrogen dioxide Ratio**

Since the emission of HCHO and NO$_2$ varies significantly with the seasons across the globe (e.g., Smedt et al., 2015; Kumar et al., 2020; Goldberg et al., 2021; Wang et al., 2017; Surl et al., 2018; Guan et al., 2021), understanding the seasonal changes in FNR is also crucial for comprehending shifts in ozone photochemical regimes. In this regard, using the methodology described in Section 4, we extracted the seasonal changes in transition limits for the major urban and semi-urban regions shown in Figure 8 and summarized in Table 4. Figure 12 illustrates the seasonal variation of estimated FNR from both OMI data and model simulations across these key urban regions. In general, all regions exhibit distinct seasonal variations in transition limits (Table 4). Previously

36

652 reported transition limits over the US (2-5 : Johnson et al., 2024; 1.1-4 : Schroeder et al., 2017)

653 and China .6-1.5/1.25-2.39 (Chen et al., 2023) during summer season are also compared with our

654 model estimates. The estimated FNR values from the ECHAM6-HAMOZ simulations shows fair

655 agreement over both the locations (0.4-4.6 at US and 0.58-2.56 at China) with some minor

656 differences. These minor discrepancy in the estimated FNR could be due to difference in the

657 chosen location, time period and dataset used. Chen et al. (2023) has also reported that the

658 transition limits significantly depends on the region considered for the analysis.

659 Table 4. Seasonal mean estimated values of the tropospheric $HCHO/NO_2$ columns threshold ratios

660 from ECHAM6-HAMMOZ model control simulation to identify the NOx and VOC sensitive

661 regimes across regions mentioned in Figure 8. The FNR less than the lower limit indicates VOC-

662 limited, and that higher than the upper limit indicates NOx-limited regimes.

Sr. No.	Regions	Transition limits							
		DJF		MAM		JJA		SON	
1	US	0.48	1.04	0.49	1.15	0.49	4.69	0.45	1.39
2	Brazil	2.93	7.79	2.93	6.66	2.93	6.02	3.12	8.44
3	European Union	0.33	1.13	0.33	1.17	0.33	3.32	0.3	1.45
4	Central Africa	2.95	7.26	2.92	5.66	2.93	6.56	3.14	7.06
5	India	2.23	3.91	2.22	9.19	2.22	5.76	2.27	5.29
6	China	0.56	1.85	0.57	1.86	0.58	2.56	1.14	2.01
7	South Australia	1.1	5.54	1.09	2.3	1.09	1.82	1.12	3.93

663

664   Based on the threshold values depicted in Table 4 and the mean FNR in Figure 12, the seasonal

665   change in ozone photochemical regimes over the key regions associated with the different emission

666   scenarios are assessed. In the CTL simulation (Figure 12e-h), the US, Europe, and China are found

667   to be in the transition regime, while all other regions are NOx-limited during winter. In spring

668   every region except India remains NOx-limited, with India transitioning into the transition regime.

669   During summer and autumn, all regions shift to a NOx-limited condition. We further compared

670   the model-estimated regional FNR from the CTL simulation with the OMI-derived FNR shown in

671   Figure 12a-d. The ozone photochemical regimes inferred from both OMI and the model show

672   consistent results except during winter. During winter, US, Europe and China are NOx limited in

673   OMI and our model shows them as the transition regimes.

674   Doubling NOx (DNOx) leads to a shift to a VOC-limited regime in all regions except Africa and

675   Australia during winter, spring, and autumn (Figure 11i-l). The relatively high VOC contributions

676   in Africa and Australia likely keep these regions in the transition regime. During summer, the US,

677   Europe, Africa and Australia transform to the transition regimes, while all other regions remain

678   VOC-limited. In both the DVOC and HNOx scenarios (Figure 11m-t), ozone photochemical

679   regimes show no seasonality. All regions consistently exhibit a NOx-limited regime throughout

680   all seasons. In the HVOC simulation (Figure 11u-x), the US, Europe, and China are in transition

681   regimes, while all other regions become NOx-limited during winter. India remains in a transition

682   regime during all other seasons, whereas other regions consistently exhibit NOx-limited

683   conditions.
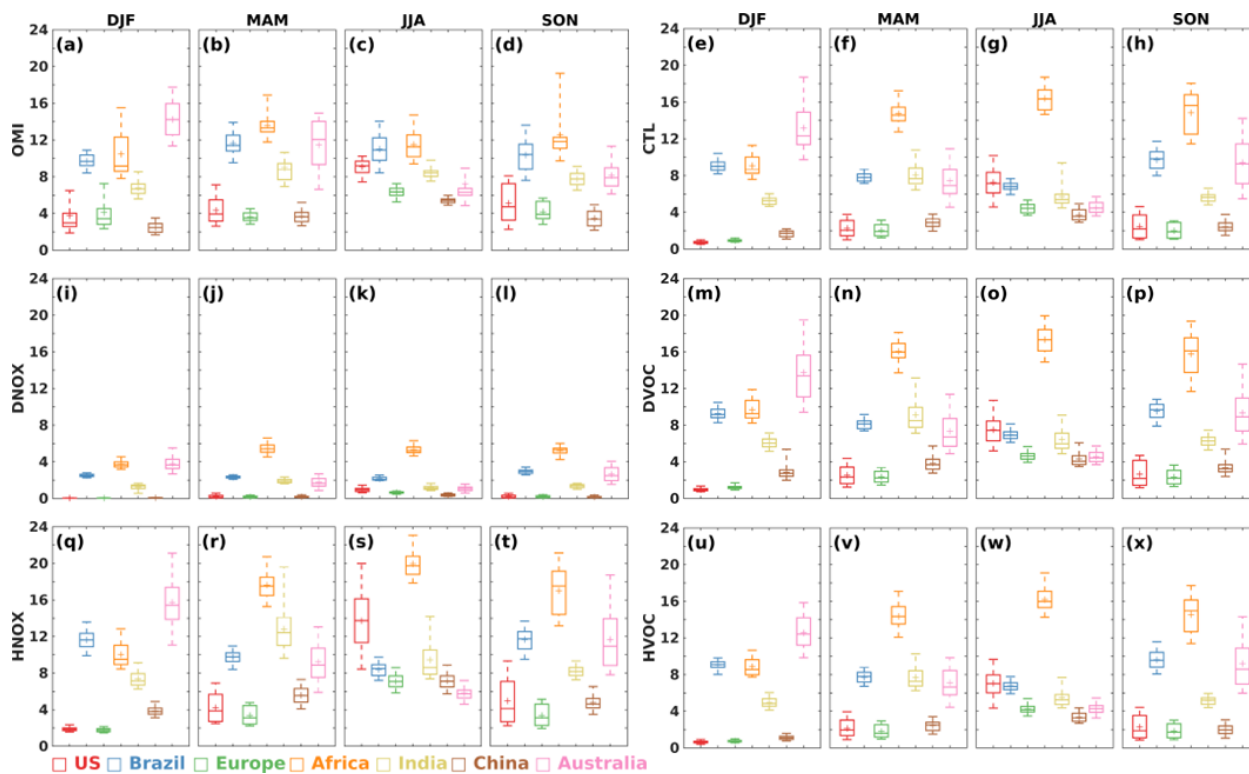
Figure 12: Box and whisker plot illustrating the long-term seasonal average FNR over the regions depicted in Fig.7. Box represents 25 and 75 percentile and whisker represents 5 and 95 percentile. The plus marker represents the mean and the horizontal bar represents the 1 and 99 percentile.

6. Influence of NOx and VOCs emissions on trends of Formaldehyde to Nitrogen dioxide Ratio

To understand the temporal evolution of ozone photochemical regimes associated with different emission scenarios, trend analysis is carried out on FNR. Figure 13 illustrates trends of FNR during the period 1998-2020 from CTL, DNOx, DVOC, HNOx, and HVOC simulations. In CTL simulation, decreasing (negative) trends in FNR are seen over the Asian region (0.4-1.2 decade^{-1}) Sand an increasing (positive) trend in Europe (0.2 decade^{-1}) and the US (0.8-1.4 decade^{-1}) (Fig. 13a). These observed trends in FNR are mainly driven by the region-specific trends on HCHO and

39

697   NO$_2$ (Figure 6). Figure 6 shows a higher positive trend in NO$_2$ than in HCHO in the Asia region,

698   causing an overall decreasing trend in FNR, indicating a tendency towards VOC-limited regimes.

699   Whereas, over the US and Europe, there is a higher negative trend in NO$_2$ than HCHO, causing a

700   positive trend in FNR. indicating a tendency towards a NOx-limited regime. A recent study by

701   Elshorbany et al. (2024) also reported a significant positive trend over Europe and the US and a

702   negative trend over Asia using the OMI-based tropospheric column - HCHO/NO$_2$ ratio. Further,

703   lLong-term column measurements of HCHO and NO$_2$ from OMI over India and China have

704   revealed an increasing trend in NO$_2$ compared to that of HCHO, causing a decreasing trend in FNR

705   over these regions (Mahajan et al., 2015; Jin and Holloway, 2015).

706

707   DNOx simulation (Figure 13b) shows a similar pattern in spatial trend as that of CTL simulation

708   (Fig 13a). However, the magnitude of this trend is less than that of the CTL. For example, a weak

709   positive trend is noted in the US and Europe (0.2-0.4 decade^{-1}), while trends over India, and China

710   are negative (0.2 - 0.4 decade^{-1}) in DNOx than CTL. (Fig. 12b). On the contrary, the magnitude

711   of positive trend over Canada and negative trend over central Africa increased in DNOx emission.

712   This indicates that Canada and central Africa have a tendency to become NOx-limited and VOC-

713   limited, respectively.

714

715   In DVOC simulations, trends are increasing over the US, Canada, and Europe compared to the

716   CTL (Fig. 13a and 13c). A notable change is observed over the Middle East and Amazon, where

717   trends become more negative and positive, respectively, compared to CTL. While, the negative

718   trends over Australia in the CTL become positive in the DVOC simulation. In HNOx simulations

719   (Fig. 13d), the positive trends are higher over the US, Europe and Amazon, while negative trends

720   prevail over India, China and Australia. The observed global trends are relatively stronger in the

721   HNOx simulation compared to all other simulations (Fig. 13). Meanwhile, in HVOC simulation,

722   marginal changes are noted globally compared to CTL. The most pronounced change in the FNR

723   trend is observed over West Australia, where the negative trend in CTL becomes increasingly

724   positive in HVOC (Fig. 13e). Figure 11f clearly shows that the trend in FNR is always negative

725   over India and China for all the simulations, indicating that these regions have a tendency to

726   become VOC-limited, while the positive trends over Europe, North America and Amazon show a

727   tendency to become more NOx-limited. Further, Figures 5 and 12 show that the relation between

728   trends in FNR and ozone exhibits a nonlinearity. For example, even though FNR shows a negative

729   trend over India and China for all the simulations, the TCO trend depends on the specific emission

730   scenario.
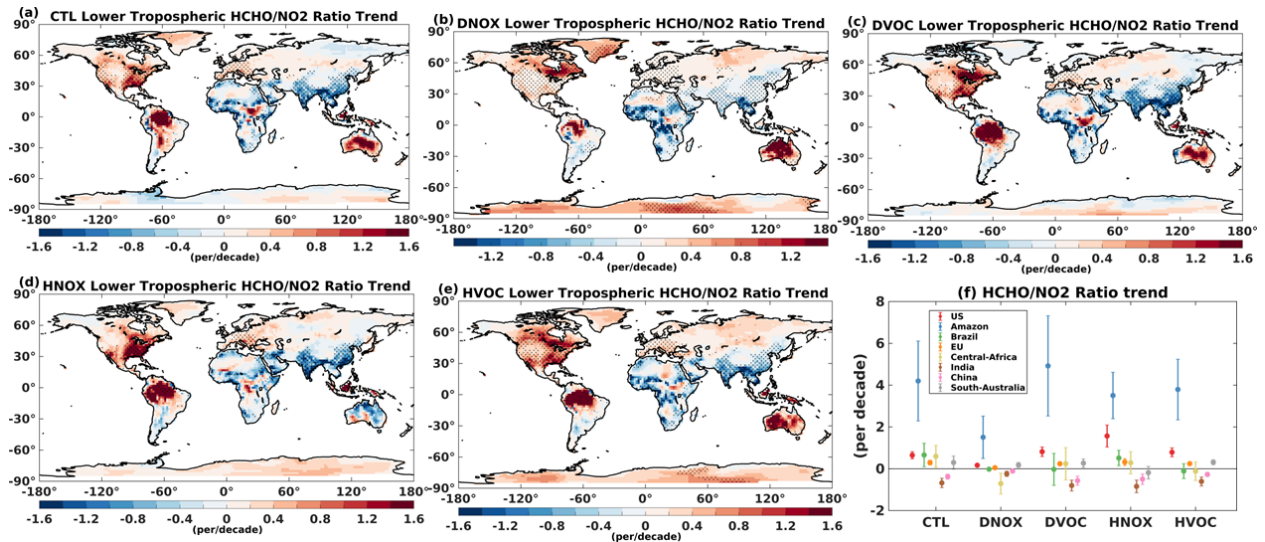
731

732   Figure 13: Trends in the lower tropospheric (surface - 700 hPa) HCHO/NO$_2$ ratio during 1998 -

733   2020 from ECHAM6-HAMMOZ simulations for (a) for CTL, (b) DNOx, (c) DVOC, (d) HNOx,

734   (e) HVOC simulations. The stippled region indicates the trend significant at 95% confidence. (f)

735   scatter plot illustrating the long-term trend and standard deviation over the regions depicted in

736   Fig.9.

737

738   **6. Tropospheric ozone radiative effects**

739   The impact of emission changes on the tropospheric ozone radiative effect (TO3RE) is estimated

740   using the ECHAM6 model output and a radiative kernel method (see data and model experiments).

741   The estimated TO3RE for different model simulations are shown in Figure 14. In the CTL

742   simulations (Fig. 14a), high TO3RE is noted over North Africa and the Middle East region in NH

743   (2.2 $W.m^{-2}$, while in SH, it is over Australia and South Africa (1.2 $W.m^{-2}$). The global mean area

744   weighted average TO3RE estimated from the CTL simulation is 1.21 $W.m^{-2}$ (1998-2020, WMO

745   tropopause). TO3RE estimates from TES measurements (2005-2009) also show a peak of 1.0

746    $W.m^{-2}$ in northern Africa, the Mediterranean, and the Middle East in June–July–August (Bowman

747   et al. 2013). Recently, Pope et al. (2024) have reported TO3RE estimates from IASI-SOFID, IASI-

748   FORLI, and IASI-IMS for the period 2008 - 2017. The values reported by Pope et al (2024) are

749   comparable with our CTL simulation (e.g. IASI-FORLI: 1.23 $W.m^{-2}$, IASI-SOFRID: 1.21$W.m^{-2}$,

750   IASI-IMS: 1.21 $W.m^{-2}$). The minor differences in the estimated global mean TO3RE from the

751   model and satellites are due to different time periods of observations/simulations.

752

753 The anomalies of TO3RE from DNOx-CTL simulations are shown in Figure 14b. Doubling of

754 NOx emission causes an enhancement in TO3RE by 0.36 W.m^{-2} compared to the CTL simulation.

755 It shows a peak over the Middle East and adjacent North Africa (0.7 W.m^{-2}). A similar peak over

756 this region is also seen in the CTL simulation. Doubling of VOC emissions enhances global mean

757 TO3RE by 0.01 W.m^{-2}, which is smaller than the doubling of NOx (Fig. 14b and 14c). TCO

758 enhancement for doubling NOx is also higher than doubling VOC (see Fig.3). DVOC-CTL

759 simulations (Fig. 14 c) show a peak over the Arctic (0.02 W.m^{-2}). The TO3RE anomalies are

760 negative between 30°N-30°S. The negative anomalies in TO3RE between 30°S-30°N (Fig. 14c)

761 can be attributed to negative anomalies of TCO (Fig. 3h).

762

763 The reduction of NOx emission by 50% reduced global mean TO3RE by -0.12 W.m^{-2} than CTL

764 (see table 3). The anomalies in TO3RE from HNOx-CTL simulations (Fig. 14d) show negative

765 anomalies all over the globe, with a strong decrease over the Middle East and adjacent North Africa

766 (-0.25 W.m^{-2}). Figures 14b and 14d show that the effect of enhancement/reduction of NOx

767 emission is high over the Middle East and adjacent North Africa. The reduction of VOC emission

768 by 50% reduced global mean TO3RE by -0.03 W.m^{-2} than CTL simulations (Fig. 14e). HVOC -

769 CTL simulations show negative anomalies of TO3RE between 40°S - 40°N and positive 0.015

770 W.m^{-2} (low confidence) over mid-high latitudes in NH and SH. From Figure 14, it is interesting

771 to note that the magnitude of TO3RE and its response to emission change is pronounced over the

772 Middle East compared to all other regions. Figure 14f indicated that impacts of NOx emission

773 changes are larger than VOC.

774

775

776

777

778

779
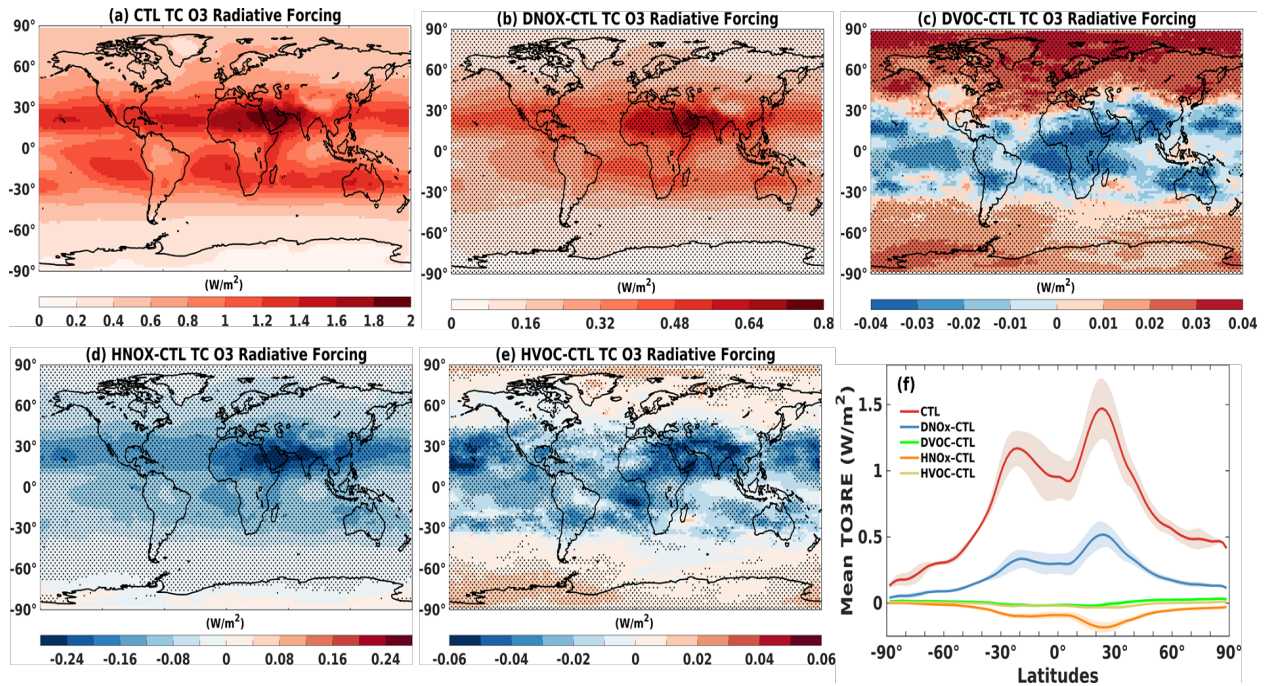
Figure 14: Tropospheric Ozone radiative effects (TO3RE) (W.m^{-2}) for (a) CTL, (b) anomalies from DNOx - CTL, (c) anomalies from DVOC - CTL, (d) anomalies from HNOx-CTL,(e) anomalies from HVOC - CTL simulations. Stippled regions in Figures (b-e) indicate RE significant at 95 % confidence level, (f) zonal mean TO3RE (W.m^{-2}) from CTL, DNOx - CTL, DVOC - CTL, HNOx-CTL, HVOC - CTL, shades indicates standard deviation.

44

785

7 Conclusions

In this study we report variation of tropospheric ozone levels, trends, photochemical regimes and radiative effect using the state-of-the-art ECHAM6-HAMMOZ chemistry-climate model simulations from 1998 to 2020. The model simulations are validated against multiple satellite observations. Our analysis shows that

(1) The model underestimates global mean TCO by 15.3 ppb than OMI/MLS, by 1.7 ppb than IASI-SOFRID.

(2) The estimated global mean trend in TCO from CTL for the period 1998-2020 is 0.94 [-0.91;4.5] ppb.decade^{-1}. Trend estimates from OMI/MLS (1.41 [-2.15 4.54] ppb.decade^{-1}) for the period Oct 2004 to Dec 2020 show good agreement with CTL (1.86 [-2.7;4.6] ppb.decade^{-1}) for the same period. It has to be noted that IASI-SOFRID documents slightly negative trends (0.01 [-3.9 ;7.1] ppb.decade^{-1}) over the globe. The trends discrepancy between UV-Vis (mostly positive trends) and IR sensors (negative trends) was already documented in Gaudel et al. (2018).

(3) DNOx-CTL simulations show positive trends are seen over Europe, the US, Africa, and South America, with a global mean increase in TCO trend by 1.23 [-5.32; 5.76] ppb.decade^{-1} and negative trends in surface ozone and TCO (-0.4 to -2 ppb.decade^{-1}) over India, China, and Australia.

804   (4) Compared to DNOx-CTL, DVOC-CTL simulations show a marginal enhancement in TCO

805   global mean trend (by 0.5 [-0.85; 1.93] ppb.decade^{-1}). HNOx - CTL and HVOC - CTL

806   simulations show decreases in the global mean TCO trends by 0.38 [-1.96; 1.64] ppb.decade^{-1}

807   and 0.42 [-0.96;1.61] ppb.decade^{-1}, respectively.

808   (5) The spatial distribution of ozone anomalies shows that enhancement in ozone is nearly 16

809   times less in DVOC simulation than that of doubling NO$_X$ simulation. The largest increase in

810   surface ozone concentration for DVOC is observed over Indo-Gangetic Plains, Eastern China

811   and the eastern United States (4-6 ppb), where a decrease in ozone is observed in the DNOx

812   simulation. This decrease (increase) in ozone with an increase in NOx (VOC) indicates that

813   these regions are VOC-limited.

814   (6) The FNR over the major urban and semi-urban regions shows that the transition from

815   VOC-limited to NOx-limited happens suddenly in response to changes in the emission of

816   NOx/VOC over the US and China. Whereas this transition region is wider in Central Africa.

817   Most polluted cities/industrialized areas in the US, Canada, Europe, west Russia, East China,

818   Korea and Japan are identified with a low FNR, indicating VOC limited (FNRs <2).

819   Meanwhile, NOx-limited regimes (largest FNR values >5) are primarily found in tropical

820   rainforests, savannas, and arid climates.

821   (7) The DNOx simulation shows a notable change in the spatial extent of VOC-limited

822   regimes, particularly in the Northern Hemisphere (NH). While the southern hemisphere (SH)

823   exhibits minimal change in the spatial extent of VOC-limited regimes.

824　　(8) DVOC simulations reveal persistent VOC-limited regimes over Western Europe, with

825　　moderate FNR values indicating a transition to NOx-limited regimes across most of the

826　　Northern Hemisphere. Comparing CTL and HNOx simulations globally shows a shift from

827　　VOC to NOx-limited regimes.

828　　(9) Comparison of all the emission simulations, DNOx and HNOx simulations significantly

829　　influence the shift in ozone photochemical regimes compared to DVOC and HVOC

830　　simulations, highlighting the global sensitivity of ozone photochemistry to NOx emissions

831　　changes.

832　　(10) Trends estimated from modeled FNR are negative over India and China in all the

833　　simulations, indicating that these regions have a tendency to become VOC-limited, while the

834　　positive trends over Europe, North America and Amazon, indicating a tendency to become

835　　more NOx-limited.

836　　(11) The trends in FNR are negative over India and China in all simulations. However, the

837　　trends in TCO are positive in DVOC - CTL and HVOC - CTL simulations and negative in

838　　DNOx - CTL and HNOx - CTL .

839　　(12) The tropospheric ozone radiative effects (TO3RE) in DNOx - CTL and DVOC - CTL

840　　show an increase in TO3RE by 0.36 $W.m^{-2}$ and 0.01 $W.m^{-2}$ respectively. However, HNOx-

841　　CTL and HVOC-CTL show reduction in the global mean TO3RE by -0.12 $W.m^{-2}$ and -0.03

842　　$W.m^{-2,}$ respectively.

843   (13) We show that anthropogenic NOx emissions have a higher impact on tropospheric ozone

844   levels, trends and radiative effect than VOC emissions globally.

845   **Author's contribution**: SF and YE initiated the manuscript. SF made the model simulations.
846   VS and SC did analysis. satellite data sets are provided by JZ, BB, EF, IG, ID, MR, IS. All
847   authors contributed to writing.

848

849   **Data availability**

850   Available from the TOAR FTP server

851   **Code availability**

852   Available from the corresponding author upon reasonable request.

853

854   **References:**

855   Acdan, J. J. M., Pierce, R. B., Dickens, A. F., Adelman, Z., and Nergui, T.: Examining TROPOMI
856   formaldehyde to nitrogen dioxide ratios in the Lake Michigan region: implications for ozone
857   exceedances, Atmos. Chem. Phys., 23, 7867–7885, https://doi.org/10.5194/acp-23-7867-2023,
858   2023.

859   Adame J.A., Gutierrez-Alvarez I., Cristofanelli P. and Notario A. and Bogeat J.A.and Bolivar
860   J.P.and Yela M., Surface ozone trends at El Arenosillo observatory from a new perspective,
861   Environmental Research, Volume 214, Part 1, November 2022, 113887, DOI:
862   10.1016/j.envres.2022.113887

863   Alvarado, L. M. A., Richter, A., Vrekoussis, M., Hilboll, A., Kalisz Hedegaard, A. B., Schneising,
864   O., and Burrows, J. P.: Unexpected long-range transport of glyoxal and formaldehyde observed
865   from the Copernicus Sentinel-5 Precursor satellite during the 2018 Canadian wildfires, Atmos.
866   Chem. Phys., 20, 2057–2072, https://doi.org/10.5194/acp-20-2057-2020, 2020.

867   Anderson, D. C., Nicely, J. M., Wolfe, G. M., Hanisco, T. F., Salawitch, R. J., Canty, T. P., Zeng,
868   G. (2017). Formaldehyde in the tropical western Pacific: Chemical sources and sinks, convective
869   transport, and representation in CAM-Chem and the CCMI models. *Journal of Geophysical*
870   *Research: Atmospheres*, 122, 11,201–11,226. https://doi.org/10.1002/2016JD026121

871   Barret, B., Gouzenes, Y., Le Flochmoen, E., & Ferrant, S. (2021). Retrieval of Metop-A/IASI N2O
872   profiles and validation with NDACC FTIR data. Atmosphere, 12(2), 219.

873   Barret, B., Le Flochmoen, E., Sauvage, B., Pavelin, E., Matricardi, M., & Cammas, J. P. (2011).
874   The detection of post-monsoon tropospheric ozone variability over south Asia using IASI data.
875   Atmospheric Chemistry and Physics, 11(18), 9533-9548.

876   Beig, G., & Singh, V. (2007). Trends in tropical tropospheric column ozone from satellite data and
877   MOZART model. Geophysical research letters, 34(17).

878   Borbas, E. E. and B. C. Ruston, 2010. The RTTOV UWiremis IR land surface emissivity module.
879   Mission Report EUMETSAT NWPSAF-MO-VS-042. http://nwpsaf.eu/vs_reports/nwpsaf-mo-vs-
880   042.pdf

881   Bowman, K. W., Shindell, D. T., Worden, H. M., Lamarque, J. F., Young, P. J., Stevenson, D. S.,
882   Qu, Z., de la Torre, M., Bergmann, D., Cameron-Smith, P. J., Collins, W. J., Doherty, R., Dalsøren,
883   S. B., Faluvegi, G., Folberth, G., Horowitz, L. W., Josse, B. M., Lee, Y. H., MacKenzie, I. A.,
884   Myhre, G., Nagashima, T., Naik, V., Plummer, D. A., Rumbold, S. T., Skeie, R. B., Strode, S. A.,
885   Sudo, K., Szopa, S., Voulgarakis, A., Zeng, G., Kulawik, S. S., Aghedo, A. M., and Worden, J. R.:
886   Evaluation of ACCMIP outgoing longwave radiation from tropospheric ozone using TES satellite
887   observations, Atmos. Chem. Phys., 13, 4057– 4072, https://doi.org/10.5194/acp-13-4057-2013,
888   2013.

889   Chang, C. -Y., Faust, E., Hou, X., Lee, P., Kim, H. C., Hedquist, B. C., and Liao, K. -J.:
890   Investigating ambient ozone formation regimes in neighboring cities of shale plays in the northeast
891   United States using photochemical modeling and satellite retrievals, Atmos. Environ., 142, 152–
892   170. doi:10.1016/j.atmosenv.2016.06.058, 2016.

893   Chen, Y., Wang, M., Yao, Y., Zeng, C., Zhang, W., Yan, H., Gao P., Fan L., Ye, D. (2023).
894   Research on the ozone formation sensitivity indicator of four urban agglomerations of China using
895   Ozone Monitoring Instrument (OMI) satellite data and ground-based measurements. *Science of*
896   *The Total Environment*, *869*, 161679.

897   Chu Sophie N., Sands S, Tomasik M. R., Lee P. S., and McNeill V. F., Ozone
898   Oxidation of Surface−Adsorbed Polycyclic Aromatic Hydrocarbons:
899   Role of PAH−Surface Interaction, J. Am. Chem. Soc. 2010, 132, 45, 15968−
900   15975, https://doi.org/10.1021/ja1014772

901   Cohen, Y., Petetin, H., Thouret, V., Marécal, V., Josse, B., Clark, H., Sauvage, B., Fontaine, A.,
902   Athier, G., Blot, R., Boulanger, D., Cousin, J.-M., and Nédélec, P.: Climatology and long-term

903 evolution of ozone and carbon monoxide in the upper troposphere–lower stratosphere (UTLS) at
904 northern midlatitudes, as seen by IAGOS from 1995 to 2013, Atmos. Chem. Phys., 18, 5415–5453,
905 https://doi.org/10.5194/acp-18-5415-2018, 2018.

906 Cooper O. R, Parrish D. D., Ziemke J., Balashov N. V., Cupeiro M.,. Galbally I. E, Gilge S.,
907 Horowitz L, Jensen N. R., Lamarque J.-F., Naik V., Oltmans S. J., Schwab J., Shindell D. T.,
908 hompsonA. M. T, Thouret V., Wang Y., Zbinden R. M., Global distribution and trends of
909 tropospheric ozone: An observation-based review, Collections: Knowledge Domain: Atmospheric
910 Science, *Elementa: Science of the Anthropocene* (2014) 2: 000029,
911 https://doi.org/10.12952/journal.elementa.000029

912 Cuesta, J., Costantino, L., Beekmann, M., Siour, G., Menut, L., Bessagnet, B., ... & Eremenko, M.
913 (2022). Ozone pollution during the COVID-19 lockdown in the spring of 2020 over Europe,
914 analysed from satellite observations, in situ measurements, and models. *Atmospheric Chemistry*
915 *and Physics*, *22*(7), 4471-4489.

916 Cuesta, J., Eremenko, M., Liu, X., Dufour, G., Cai, Z., Höpfner, M., ... & Flaud, J. M. (2013).
917 Satellite observation of lowermost tropospheric ozone by multispectral synergism of IASI thermal
918 infrared and GOME-2 ultraviolet measurements over Europe. Atmospheric Chemistry and
919 Physics, 13(19), 9675-9693.

920 Cuesta, J., Eremenko, M., Liu, X., Dufour, G., Cai, Z., Höpfner, M., ... & Flaud, J. M. (2013).
921 Satellite observation of lowermost tropospheric ozone by multispectral synergism of IASI thermal
922 infrared and GOME-2 ultraviolet measurements over Europe. *Atmospheric Chemistry and Physics*,
923 *13*(19), 9675-9693.

924 Cuesta, J., Kanaya, Y., Takigawa, M., Dufour, G., Eremenko, M., Foret, G., ... & Beekmann, M.
925 (2018). Transboundary ozone pollution across East Asia: daily evolution and photochemical
926 production analysed by IASI+ GOME2 multispectral satellite observations and models.
927 *Atmospheric Chemistry and Physics*, *18*(13), 9499-9525.

928 De Smedt, I., Stavrakou, T., Hendrick, F., Danckaert, T., Vlemmix, T., Pinardi, G., ... & Van
929 Roozendael, M. (2015). Diurnal, seasonal and long-term variations of global formaldehyde
930 columns inferred from combined OMI and GOME-2 observations. *Atmospheric Chemistry and*
931 *Physics*, *15*(21), 12519-12545.

932 Domenico Taraborrelli, David Cabrera-Perez2 , Sara Bacer , Sergey Gromov , Jos Lelieveld , Rolf
933 Sander , and Andrea PozzerI, Influence of aromatics on tropospheric gas-phase composition ,
934 Atmos. Chem. Phys., 21, 2615–2636, 2021 https://doi.org/10.5194/acp-21-2615-2021

935 Duncan, B. N., Lamsal, L. N., Thompson, A. M., Yoshida, Y., Lu, Z., Streets, D. G. Pickering, K.
936 E. (2016). A space-based, high-resolution view of notable changes in urban NOx pollution around
937 the world (2005–2014). Journal of Geophysical Research: Atmospheres, 121, 976–996.

938 Duncan, B., Yoshida, Y., Olson, J., Sillman, S., Martin, R., Lamsal, L., Hu, Y., Pickering, K.
939 Retscher, D. Allen, D., and Crawford, J.: Application of OMI observations to a space-based
940 indicator of NOx and VOC controls on surface ozone formation, Atmos. Environ., 44, 2213–2223,
941 https://doi.org/10.1016/j.atmosenv.2010.03.010, 2010.

942 Edwards, J. M. and Slingo, A.: Studies with a flexible new radiation code. I: Choosing a
943 configuration for a large scale model, Q. J. Roy. Meteor. Soc., 122, 689–719,
944 https://doi.org/10.1002/qj.49712253107, 1996.

945 Elshorbany, Y., Ziemke, J., Strode, S., Petetin, H., Miyazaki, K., De Smedt, I., ... & Huang, M.
946 (2024). Tropospheric Ozone Precursors: Global and Regional Distributions, Trends and
947 Variability. EGU sphere, 2024, 1-57.

948 Emmons, L. K., Apel, E. C., Lamarque, J.-F., Hess, P. G., Avery, M., Blake, D., Brune, W.,
949 Campos, T., Crawford, J., DeCarlo, P. F., Hall, S., Heikes, B., Holloway, J., Jimenez, J. L., Knapp,
950 D. J., Kok, G., Mena-Carrasco, M., Olson, J., O'Sullivan, D., Sachse, G., Walega, J., Weibring, P.,
951 Weinheimer, A., and Wiedinmyer, C.: Impact of Mexico City emissions on regional air quality
952 from MOZART-4 simulations, Atmos. Chem. Phys., 10, 6195–6212, https://doi.org/10.5194/acp-
953 10-6195-2010, 2010.

954 EPA, O. U. Air Pollutant Emissions Trends Data. 2023. https://www.epa.gov/air-emissions-
955 inventories/air-pollutant-emissions-trends-data

956 Eyring, V., J. M. Arblaster, I. Cionni, J. Sedláček, J. Perlwitz, P. J. Young, S. Bekki, D. J.
957 Bergmann, P. Cameron-Smith, W. J. Collins, G. Faluvegi, D. Shindell, et al. (2013), Long-term
958 ozone changes and associated climate impacts in CMIP5 simulations, J. Geophys. Res., 118, 5029-
959 5060, doi:10.1002/jgrd.50316

960 Fadnavis S., Chavan P., Joshi A., Sonbawne S.M., Acharya A., Devara P.C.S., Rap A., Ploeger F.,
961 Müller R., Tropospheric warming over the northern Indian Ocean caused by South Asian
962 anthropogenic aerosols: possible impact on the upper troposphere and lower stratosphere,
963 Atmospheric Chemistry and Physics, 22, June 2022, DOI:10.5194/acp-22-7179-2022 , 7179–719.

964 Fadnavis S., Heinold B., Sabin T.P., Kubin A., Huang K., Rap A., Müller R., Air pollution
965 reductions caused by the COVID-19 lockdown open up a way to preserve the Himalayan glaciers.,
966 Atmospheric Chemistry and Physics, 23, September 2023, DOI:10.5194/acp-23-10439-2023,
967 10439-10449

968 Fadnavis S., Müller R., Chakraborty T., Sabin T.P., Laakso A., Rap A., Griessbach S., Vernier
969 J.V., Tilmes S., The role of tropical volcanic eruptions in exacerbating Indian droughts, Scientific
970 Reports, 11: 2714, 2021a, DOI:10.1038/s41598-021-81566-0, 1-13.,

971 Fadnavis S., Müller R., Kalita G., Rowlinson M., Rap A., Li J-L.F., Gasparini B., Laakso A.,
972 Impact of recent changes in Asian anthropogenic emissions of SO2 on sulfate loading in the upper
973 troposphere and lower stratosphere and the associated radiative changes, Atmospheric Chemistry
974 and Physics, 19, 2019a, DOI:10.5194/acp-19-9989-2019, 9989–10008.

975 Fadnavis S., Sabin T.P., Rap A., Müller R., Kubin A., Heinold B., The impact of COVID-19
976 lockdown measures on the Indian summer monsoon , Environmental Research Letters, 16: 074054,
977 July 2021b, DOI: 10.1088/1748-9326/ac109c, 1-13

978 Fadnavis S., Sabin T.P., Roy C., Rowlinson M., Rap A., Vernier J.-P., Sioris C.E., Elevated aerosol
979 layer over South Asia worsens the Indian droughts, Scientific Reports, 9:10268, 2019b,
980 DOI:10.1038/s41598-019-46704-9, 1-11

981

982 Fiore Arlene Met al 2022 Understanding recent tropospheric ozone trends in the context of large
983 internal variability: a new perspective from chemistry-climate model ensembles, Environ. Res.:
984 Climate 1 025008, DOI 10.1088/2752-5295/ac9cc2

985 Fiore, A. M., Hancock, S. E., Lamarque, J. F., Correa, G. P., Chang, K. L., Ru, M., ... & Ziemke,
986 J. R. (2022). Understanding recent tropospheric ozone trends in the context of large internal
987 variability: a new perspective from chemistry-climate model ensembles. Environmental Research:
988 Climate, 1(2), 025008.

989 Fleming, Z. L., Doherty, R. M., Von Schneidemesser, E., Malley, C. S., Cooper, O. R., Pinto, J.
990 P., ... & Feng, Z. (2018). Tropospheric Ozone Assessment Report: Present-day ozone distribution
991 and trends relevant to human health. Elem Sci Anth, 6, 12.

992 Gaudel, A., Cooper, O. R., Ancellet, G., Barret, B., Boynard, A., Burrows, J. P., ... & Ziemke, J.
993 (2018). Tropospheric Ozone Assessment Report: Present-day distribution and trends of
994 tropospheric ozone relevant to climate and global atmospheric chemistry model evaluation. Elem
995 Sci Anth, 6, 39.

996 Gaudel, A., I. Bourgeois, M. Li, O. Cooper, K.-L. Chang, B. Sauvage, J. R. Ziemke, A. Thompson,
997 R. Stauffer, and N. Smith, In-situ and satellite-based quantification of tropical tropospheric ozone,
998 Atmos. Chem. Phys., in review, 2024.

999 Glissenaar, I. A., Anglou, I., Boersma, K. F., & Eskes, H. (2024). ESA CCI+ TROPOMI L3
1000 monthly mean NO2 columns [Data set]. Royal Netherlands Meteorological Institute (KNMI).
1001 https://doi.org/10.21944/CCI-NO2-TROPOMI-L3

1002 Goldberg, D. L., Anenberg, S. C., Kerr, G. H., Mohegh, A., Lu, Z., and Streets, D. G.: TROPOMI
1003 NO2 in the United States: A Detailed Look at the Annual Averages, Weekly Cycles, Effects of
1004 Temperature, and Correlation With Surface NO2 Concentrations, Earth's Future, 9,
1005 e2020EF001665, https://doi.org/10.1029/2020EF001665, 2021

1006 Griffiths, P. T., Murray, L. T., Zeng, G., Shin, Y. M., Abraham, N. L., Archibald, A. T., Deushi,
1007 M., Emmons, L. K., Galbally, I. E., Hassler, B., Horowitz, L. W., Keeble, J., Liu, J., Moeini, O.,
1008 Naik, V., O'Connor, F. M., Oshima, N., Tarasick, D., Tilmes, S., Turnock, S. T., Wild, O., Young,
1009 P. J., and Zanis, P.: Tropospheric ozone in CMIP6 simulations, Atmos. Chem. Phys., 21, 4187–
1010 4218, https://doi.org/10.5194/acp-21-4187-2021, 2021.

1011 Guan, J., Jin, B., Ding, Y., Wang, W., Li, G., & Ciren, P. (2021). Global surface HCHO
1012 distribution derived from satellite observations with neural networks technique. *Remote Sensing*,
1013 *13*(20), 4055

1014 Guerreiro, C. B. B., Foltescu, V., & de Leeuw, F. (2014). Air quality status and trends in Europe.
1015 Atmospheric Environment, 98(c), 376–384. https://doi.org/10.1016/j.atmosenv.2014.09.017

1016 Gulev, S. K., Thorne, P. W. (2021). Changing state of the climate system,
1017 https://doi.org/10.1002/2015JD024121

1018 IPCC, 2021: *Climate Change 2021: The Physical Science Basis. Contribution of Working Group*
1019 *I to the Sixth Assessment Report of the Intergovernmental Panel on Climate Change*[Masson-
1020 Delmotte, V., P. Zhai, A. Pirani, S.L. Connors, C. Péan, S. Berger, N. Caud, Y. Chen, L. Goldfarb,
1021 M.I. Gomis, M. Huang, K. Leitzell, E. Lonnoy, J.B.R. Matthews, T.K. Maycock, T. Waterfield,
1022 O. Yelekçi, R. Yu, and B. Zhou (eds.)]. Cambridge University Press, Cambridge, United Kingdom
1023 and New York, NY, USA, In press, doi:10.1017/9781009157896.

1024 Jin, X., & Holloway, T. (2015). Spatial and temporal variability of ozone sensitivity over China
1025 observed from the Ozone Monitoring Instrument. Journal of Geophysical Research: Atmospheres,
1026 120(14), 7229-7246.

1027 Jin, X., Fiore, A. M., Murray, L. T., Valin, L. C., Lamsal, L. N., Duncan, B., Boersma, K. F., De
1028 Smedt, I., Abad, G. G., Chance, K., and Tonnesen, G. S.: Evaluating a Space-Based Indicator of
1029 Surface Ozone-NOx-VOC Sensitivity Over Midlatitude Source Regions and Application to
1030 Decadal Trends, J. Geophys. Res.-Atmos., 122, 10439–10461,
1031 https://doi.org/10.1002/2017JD026720, 2017.

1032 Jin, X., Fiore, A., Boersma, K. F., De Smedt, I., and Valin, L.: Inferring Changes in Summertime
1033 Surface Ozone–NOx–VOC Chemistry over U.S. Urban Areas from Two Decades of Satellite and
1034 Ground-Based Observations, Environ. Sci. Technol., 54, 6518–6529,
1035 https://doi.org/10.1021/acs.est.9b07785, 2020.

1036 Johnson, M. S., Philip, S., Meech, S., Kumar, R., Sorek-Hamer, M., and Shiga, Y. P.: Insights into
1037 the long-term (2005–2021) spatiotemporal evolution of summer ozone production sensitivity in
1038 the Northern Hemisphere derived with OMI, EGUsphere [preprint],
1039 https://doi.org/10.5194/egusphere-2024-583, 2024.

1040 Kinnison, D. E., Brasseur, G. P., Walters, S., Garcia, R. R., Marsh, D. R., Sassi, F., Harvey, V. L.,
1041 Randall, C. E., Emmons, L., Lamarque, J. F., Hess, P., Orlando, J. J., Tie, X. X., Randel, W., Pan,
1042 L. L., Gettelman, A., Granier, C., Diehl, T., Niemeier, U., and Simmons, A. J.: Sensitivity of
1043 chemical tracers to meteorological parameters in the MOZART-3 chemical transport model, J.
1044 Geophys. Res.-Atmos., 112, 20302, https://doi.org/10.1029/2006JD007879, 2007

1045 Kleinman, L. I. (1994), Low and high NO_x tropospheric photochemistry, *J. Geophys. Res.*, 99(D8),
1046 16831–16838, doi:10.1029/94JD01028.

1047 Kumar, V., Beirle, S., Dörner, S., Mishra, A. K., Donner, S., Wang, Y., ... & Wagner, T. (2020).
1048 Long-term MAX-DOAS measurements of NO 2, HCHO, and aerosols and evaluation of
1049 corresponding satellite data products over Mohali in the Indo-Gangetic Plain. *Atmospheric
1050 Chemistry and Physics*, *20*(22), 14183-14235

1051 Lamarque J. F. et al., 2010. Historical (1850–2000) gridded anthropogenic and biomass burning
1052 emissions of reactive gases and aerosols: methodology and application, Atmos. Chem. Phys., 10,
1053 7017-7039, doi:10.5194/acp-10-7017-2010
1054
1055 Van Vuuren, D.P. et al., 2011. Representative concentration pathways: an overview. Climatic
1056 Change (2011) 109:5–31, DOI 10.1007/s10584-011-0148-z

1057

1058 Lamarque, J. F., Emmons, L. K., Hess, P. G., Kinnison, D. E., Tilmes, S., Vitt, F., ... & Tyndall,
1059 G. K. (2012). CAM-chem: Description and evaluation of interactive atmospheric chemistry in the
1060 Community Earth System Model. *Geoscientific Model Development*, *5*(2), 369-411.

1061 Lee, H. J., Chang, L. S., Jaffe, D. A., Bak, J., Liu, X., Abad, G. G., ... & Kim, C. H. (2022).
1062 Satellite-based diagnosis and numerical verification of ozone formation regimes over nine
1063 megacities in East Asia. *Remote Sensing*, *14*(5), 1285.

1064 Lefohn, A. S., Malley, C. S., Simon, H., Wells, B., Xu, X., Zhang, L., & Wang, T. (2017).
1065 Responses of human health and vegetation exposure metrics to changes in ozone concentration
1066 distributions in the European Union, United States, and China. Atmospheric Environment, 152,
1067 123–145, https://doi.org/10.1016/j.atmosenv.2016.12.025

1068 Lin M, Horowitz LW, Oltmans SJ, et al. Tropospheric ozone trends at Mauna Loa Observatory 18
1069 494 tied to decadal climate variability. Nature Geosci, 2014, 7: 136-143 495

1070 Lin, X., M. Trainer, and S. C. Liu (1988), On the nonlinearity of the tropospheric ozone production,
1071 *J. Geophys. Res.*, 93(D12), 15879–15888, doi:10.1029/JD093iD12p15879.

1072 Lu X, Zhang L, Liu X, et al. Lower tropospheric ozone over India and its linkage to the South 496
1073 Asian monsoon. Atmos Chem Phys, 2018, 18: 3101-3118

1074 Ma X., Huang J., Hegglin M. I., Jöckel P., and Zhao T., Causes of growing middle-upper
1075 tropospheric ozone over the Northwest Pacific region, ACPD, 20024,
1076 https://doi.org/10.5194/egusphere-2023-2411

1077 Maddox E. M. and G. L. Mullendore Determination of Best Tropopause Definition for Convective
1078 Transport Studies, Journal of the Atmospheric Sciences, 3433–3446, 2018,
1079 https://doi.org/10.1175/JAS-D-18-0032.1

1080 Mahajan, A. S., De Smedt, I., Biswas, M. S., Ghude, S., Fadnavis, S., Roy, C., & van Roozendael,
1081 M. (2015). Inter-annual variations in satellite observations of nitrogen dioxide and formaldehyde
1082 over India. Atmospheric Environment, 116, 194-201.

1083 Martin, R. V., Fiore, A. M., and Van Donkelaar, A.: Space-based diagnosis of surface ozone
1084 sensitivity to anthropogenic emissions, Geophys. Res. Lett., 31, L06120.
1085 doi:10.1029/2004GL019416, 2004.

1086 Matricardi, M., Chevallier, F., Kelly, G., & Thépaut, J. N. (2004). An improved general fast
1087 radiative transfer model for the assimilation of radiance observations. Quarterly Journal of the
1088 Royal Meteorological Society, 130(596), 153-173.

1089 Millet, D. B., Jacob, D. J., Boersma, K. F., Fu, T. M., Kurosu, T. P., Chance, K., ... & Guenther,
1090 A. (2008). Spatial distribution of isoprene emissions from North America derived from
1091 formaldehyde column measurements by the OMI satellite sensor. Journal of Geophysical
1092 Research: Atmospheres, 113(D2).

1093 Mills, G., Pleijel, H., Malley, C. S., Sinha, B., Cooper, O. R., Schultz, M. G., ... & Xu, X. (2018).
1094 Tropospheric Ozone Assessment Report: Present-day tropospheric ozone distribution and trends
1095 relevant to vegetation. Elem Sci Anth, 6, 47.

1096 Monks, P. S., Archibald, A. T., Colette, A., Cooper, O., Coyle, M., Derwent, R., Fowler, D.,
1097 Granier, C., Law, K. S., Mills, G. E., Stevenson, D. S., Tarasova, O., Thouret, V., von
1098 Schneidemesser, E., Sommariva, R., Wild, O., and Williams, M. L.: Tropospheric ozone and its
1099 precursors from the urban to the global scale from air quality to short-lived climate forcer, Atmos.
1100 Chem. Phys., 15, 8889–8973, https://doi.org/10.5194/acp-15-8889-2015, 2015.

1101 O3 (IASI+GOME2) – IASI portal: https://iasi.aeris-data.fr/o3_iago2/, last access: 28 May 2024

1102 Okamoto, S., Cuesta, J., Beekmann, M., Dufour, G., Eremenko, M., Miyazaki, K., Boonne C.,
1103 Tanimoto H., Akimoto, H. (2023). Impact of different sources of precursors on an ozone pollution
1104 outbreak over Europe analysed with IASI+GOME2 multispectral satellite observations and model
1105 simulations. *Atmospheric Chemistry and Physics*, *23*(13), 7399-7423.

1106 Pope R. J. Rap A., Pimlott M. A, Barret B., Flochmoen E. Le, Kerridge B. J., Richard Siddans,
1107 Barry G. Latter, Lucy J. Ventress, Anne Boynard, Christian Retscher, Wuhu Feng, Richard
1108 Rigby, Sandip S. Dhomse, Catherine Wespes, and Martyn P. Chipperfield, Quantifying the
1109 tropospheric ozone radiative effect and its temporal evolution in the satellite era, Atmos. Chem.
1110 Phys., 24, 3613–3626, 2024 https://doi.org/10.5194/acp-24-3613-2024

1111 Pope, R. J., Savage, N. H., Chipperfield, M. P., Arnold, S. R., & Osborn, T. J. (2014). The influence
1112 of synoptic weather regimes on UK air quality: analysis of satellite column NO2. *Atmospheric*
1113 *Science Letters*, *15*(3), 211-217.

1114 Rap, A., Richard, N. A. D., Forster, P. M., Monks, S. A., Arnold, S. R., and Chipperfield, M. P.:
1115 Satellite constraint on the tropospheric ozone radiative effect, Geophys. Res. Lett., 42, 5074– 5081,
1116 https://doi.org/10.1002/2015GL064037, 2015.

1117 Reick, C. H., Raddatz, T., Brovkin, V., and Gayler, V.: Representation of natural and
1118 anthropogenic land cover change in MPI-ESM, J. Adv. Model. Earth Sy., 5, 459–482,
1119 https://doi.org/10.1002/jame.20022, 2013.

1120 Ren, J., Guo, F., and Xie, S.: Diagnosing ozone–NO_x–VOC sensitivity and revealing causes of
1121 ozone increases in China based on 2013–2021 satellite retrievals, Atmos. Chem. Phys., 22, 15035–
1122 15047, https://doi.org/10.5194/acp-22-15035-2022, 2022.

1123 Rosanka S , Franco B. , Clarisse L , Coheur P-F , Pozzer A. , Wahner A , and Taraborrelli D., The
1124 impact of organic pollutants from Indonesian peatland fires on the tropospheric and lower

stratospheric composition, Atmos. Chem. Phys., 21, 11257–11288, 2021 https://doi.org/10.5194/acp-21-11257-2021.

Rossow, W. B. and Schiffer, R. A.: Advances in understanding clouds from ISCCP, B. Am. Meteorol. Soc., 80, 2261–2287, https://doi.org/10.1175/1520-0477(1999)080>2.0.co;2,1999

Rowlinson, M. J., Rap, A., Hamilton, D. S., Pope, R. J., Hantson, S., Arnold, S. R., Kaplan, J. O., Arneth, A., Chipperfield, M. P., Forster, P. M., and Nieradzik, L.: Tropospheric ozone radiative forcing uncertainty due to pre-industrial fire and biogenic emissions Atmos. Chem. Phys., 19, 8669–8686, https://doi.org/10.5194/acp-19-8669-2019, 2019.

Rowlinson, M. J., Rap, A., Hamilton, D. S., Pope, R. J., Hantson, S., Arnold, S. R., Kaplan, J. O., Arneth, A., Chipperfield, M. P., Forster, P. M., and Nieradzik, L.: Tropospheric ozone radiative forcing uncertainty due to pre-industrial fire and biogenic emissions, Atmos. Chem. Phys., 20, 10937–10951, https://doi.org/10.5194/acp-20-10937-2020, 2020

Saunders, R., Matricardi, M., & Brunel, P. (1999). An improved fast radiative transfer model for assimilation of satellite radiance observations. Quarterly Journal of the Royal Meteorological Society, 125(556), 1407-1425.

Schroeder, J. R., Crawford, J. H., Fried, A., Walega, J., Weinheimer, A., Wisthaler, A., ... & Tonnesen, G. S. (2017). New insights into the column CH2O/NO2 ratio as an indicator of near-surface ozone sensitivity. Journal of Geophysical Research: Atmospheres, 122(16), 8885-8907.

Schultz, M. G., Schröder, S., Lyapina, O., Cooper, O. R., Galbally, I., Petropavlovskikh, I, Von Schneidemesser, E., Tanimoto, H., Elshorbany, Y., Naja, M., Seguel, R. J., Dauert, U., Eckhardt, P., Feigenspan, S., Fiebig, M., Hjellbrekke, A., Hong, Y., Kjeld, P. C., Koide, H., . . . Zhiqiang, M. (2016). Tropospheric Ozone Assessment Report: Database and metrics data of global surface ozone observations. *Elementa: Science of the Anthropocene*, 5. https://doi.org/10.1525/elementa.244

Schultz, M. G., Schröder, S., Lyapina, O., Cooper, O. R., Galbally, I., Petropavlovskikh, I., ... & Zhiqiang, M. (2017). Tropospheric Ozone Assessment Report: Database and metrics data of global surface ozone observations. Elem Sci Anth, 5, 58.

Schultz, M. G., Stadtler, S., Schröder, S., Taraborrelli, D., Franco, B., Krefting, J., Henrot, A., Ferrachat, S., Lohmann, U., Neubauer, D., Siegenthaler-Le Drian, C., Wahl, S., Kokkola, H., Kühn, T., Rast, S., Schmidt, H., Stier, P., Kinnison, D., Tyndall, G. S., Orlando, J. J., and Wespes, C.: The chemistry–climate model ECHAM6.3-HAM2.3-MOZ1.0, Geosci. Model Dev., 11, 1695–1723, https://doi.org/10.5194/gmd-11-1695-2018, 2018.

Scott, C. E., Monks, S. A., Spracklen, D. V., Arnold, S. R., Forster, P. M., Rap, A., Aijala, M., Artaxo, P., Carslaw, K. S., Chipperfield, M. P., Ehn, M., Gilardoni, S., Heikkinen, L., Kulmala, M., Petaja, T., Reddington, C. L. S, Rizzo, L. V., Swietlicki, E., Vignati, E., and Wilson, C.: Impact on short-lived climate forcers increases projected warming due to deforestation, Nat. Commun.,9, 157, https://doi.org/10.1038/s41467-017-02412-4, 2018

Shen, L., Jacob, D. J., Zhu, L., Zhang, Q., Zheng, B., Sulprizio, M. P., Li K., Smedt I. D., Abad G. G., Cao H., Fu T.-M., Liao, H. (2019). The 2005–2016 trends of formaldehyde columns over China observed by satellites: Increasing anthropogenic emissions of volatile organic compounds and decreasing agricultural fire emissions. Geophysical Research Letters, 46(8), 4468-4475.

Sillman, S.: The use of NOy, H2O2, and HNO3 as indicators for O3-NOx-hydrocarbon sensitivity in urban locations, J. Geophys. Res. Atmos., 100, 14175-14188, doi:10.1029/94JD02953, 1995.

Sillman, S., J. A. Logan, and S. C. Wofsy (1990), The sensitivity of ozone to nitrogen oxides and hydrocarbons in regional ozone episodes, *J. Geophys. Res.*, 95(D2), 1837–1851, doi:10.1029/JD095iD02p01837.

Skeie, R.B., Myhre, G., Hodnebrog, Ø. *et al.* Historical total ozone radiative forcing derived from CMIP6 simulations. *npj Clim Atmos Sci* 3, 32 (2020). https://doi.org/10.1038/s41612-020-00131-0

Sofieva, V. F., Tamminen, J., Kyrölä, E., Mielonen, T., Veefkind, P., Hassler, B., and Bodeker, G. E.: A novel tropopause-related climatology of ozone profiles, Atmos. Chem. Phys., 14, 283–299, https://doi.org/10.5194/acp-14-283-2014, 2014.

son, M. S., Souri, A. H., Philip, S., Kumar, R., Naeger, A., Geddes, J., Judd, L., Janz, S., Chong, H., and Sullivan, J.: Satellite remote-sensing capability to assess tropospheric-column ratios of formaldehyde and nitrogen dioxide: case study during the Long Island Sound Tropospheric Ozone Study 2018 (LISTOS 2018) field campaign, Atmos. Meas. Tech., 16, 2431–2454, https://doi.org/10.5194/amt-16-2431-2023, 2023.

Souri, A. H., Choi, Y., Jeon, W., Woo, J. -H., Zhang, Q., and Kurokawa J.-i.: Remote sensing evidence of decadal changes in major tropospheric ozone precursors over East Asia, J. Geophys. Res. Atmos., 122, 2474-2492, doi:10.1002/2016JD025663, 2017.

Stadtler, S., Simpson, D., Schröder, S., Taraborrelli, D., Bott, A., & Schultz, M. (2018). Ozone impacts of gas–aerosol uptake in global chemistry transport models. *Atmospheric chemistry and physics*, *18*(5), 3147-3171.

1188 Stevens, B., Giorgetta, M., Esch, M., Mauritsen, T., Crueger, T., Rast, S., ... & Roeckner, E. (2013).
1189 Atmospheric component of the MPI-M Earth system model: ECHAM6. *Journal of Advances in*
1190 *Modeling Earth Systems*, *5*(2), 146-172.

1191 Stevenson, D. S., Dentener, F. J., Schultz, M. G., Ellingsen, K., van Noije, T. P. C., Wild, O.,
1192 Zeng, G., Amann, M., Atherton, C. S., Bell, N., Bergmann, D. J., Bey, I., Butler, T., Cofala, J.,
1193 Collins, W. J., Derwent, R. G., Doherty, R. M., Drevet, J., Eskes, H. J., Fiore, A. M., Gauss, M.,
1194 Hauglustaine, D. A., Horowitz, L. W., Isaksen, I. S. A., Krol, M. C., Lamarque, J. F., Lawrence,
1195 M. G., Montanaro, V., Muller, J. F., Pitari, G., Prather, M. J., Pyle, J. A., Rast, S., Rodriguez, J.
1196 M., Sanderson, M. G., Savage, N. H., Shindell, D. T., Strahan, S. E., Sudo, K., and Szopa, S.:
1197 Multimodel ensemble simulations of present-day and near-future tropospheric ozone, J. Geophys.
1198 Res., 111, D08301, https://doi.org/10.1029/2005jd006338, 2006.

1199 Stevenson, D. S., Dentener, F. J., Schultz, M. G., Ellingsen, K., van Noije, T. P. C., Wild, O.,
1200 Zeng, G., Amann, M., Atherton, C. S., Bell, N., Bergmann, D. J., Bey, I., Butler, T., Cofala, J.,
1201 Collins, W. J., Derwent, R. G., Doherty, R. M., Drevet, J., Eskes, H. J., Fiore, A. M., Gauss, M.,
1202 Hauglustaine, D. A., Horowitz, L. W., Isaksen, I. S. A., Krol, M. C., Lamarque, J. F., Lawrence,
1203 M. G., Montanaro, V., Muller, J. F., Pitari, G., Prather, M. J., Pyle, J. A., Rast, S., Rodriguez, J.
1204 M., Sanderson, M. G., Savage, N. H., Shindell, D. T., Strahan, S. E., Sudo, K., and Szopa, S.:
1205 Multimodel ensemble simulations of present-day and near-future tropospheric ozone, J. Geophys.
1206 Res., 111, D08301, https://doi.org/10.1029/2005jd006338, 2006.

1207 Surl, L., Palmer, P. I., & González Abad, G. (2018). Which processes drive observed variations of
1208 HCHO columns over India?. *Atmospheric Chemistry and Physics*, *18*(7), 4549-4566.

1209 Tao, M., Fiore, A. M., Jin, X., Schiferl, L. D., Commane, R., Judd, L. M., Janz, S., Sullivan, J. T.,
1210 Miller, P. J., Karambelas, A., Davis, S., Tzortziou, M., Valin, L., Whitehill, A., Civerolo, K., and
1211 Tian, Y.: Investigating changes in ozone formation chemistry during summertime pollution vents
1212 over the northeastern United States, Environ. Sci. Technol., 56, 15312–15327,
1213 https://doi.org/10.1021/acs.est.2c02972, 2022.

1214 Tarasick, D. W., Carey-Smith, T. K., Hocking, W. K., Moeini, O., He, H., Liu, J., Osman, M. K.,
1215 Thompson, A. M., Johnson, B. J., Oltmans, S. J., and Merrill, J. T.: Quantifying stratosphere-
1216 troposphere transport of ozone using balloon-borne ozonesondes, radar windprofilers and
1217 trajectory models, Atmos. Environ., 198, 496–509,
1218 https://doi.org/10.1016/j.atmosenv.2018.10.040, 2019.

1219 Veefkind, J. P., Aben, I., McMullan, K., Förster, H., de Vries, J., Otter, G., et al. (2012). TROPOMI
1220 on the ESA Sentinel-5 Precursor: A GMES mission for global observations of the atmospheric

composition for climate, air quality and ozone layer applications. Remote Sensing of Environment, 120(2012), 70–83. https://doi.org/10.1016/j.rse.2011.09.027

Vignati, E., Wilson, J., and Stier, P.: M7: An efficient size-resolved aerosol microphysics module for large-scale aerosol transport models, J. Geophys. Res.-Atmos., 109, D22202, https://doi.org/10.1029/2003jd004485, 2004

Wang, H., Lu, X., Jacob, D. J., Cooper, O. R., Chang, K.-L., Li, K., Gao, M., Liu, Y., Sheng, B., Wu, K., Wu, T., Zhang, J., Sauvage, B., Nédélec, P., Blot, R., and Fan, S.: Global tropospheric ozone trends, attributions, and radiative impacts in 1995–2017: an integrated analysis using aircraft (IAGOS) observations, ozonesonde, and multi-decadal chemical model simulations, Atmos. Chem. Phys., 22, 13753–13782, https://doi.org/10.5194/acp-22-13753-2022, 2022.

Wang, W., van der A, R., Ding, J., van Weele, M., and Cheng, T.: Spatial and temporal changes of the ozone sensitivity in China based on satellite and ground-based observations, Atmos. Chem. Phys., 21, 7253–7269, https://doi.org/10.5194/acp-21-7253-2021, 2021.

Wang, Y., Lampel, J., Xie, P., Beirle, S., Li, A., Wu, D., & Wagner, T. (2017). Ground-based MAX-DOAS observations of tropospheric aerosols, NO 2, SO 2 and HCHO in Wuxi, China, from 2011 to 2014. *Atmospheric Chemistry and Physics*, *17*(3), 2189-2215

WMO, Meteorology – A three-dimensional science, World Meteorological Organisation, Bulletin 6, (Oct), 134–138, 1957.

Young, P. J., Naik, V., Fiore, A. M., Gaudel, A., Guo, J., Lin, M. Y., ... & Zeng, G. (2018). Tropospheric Ozone Assessment Report: Assessment of global-scale model performance for global and regional ozone distributions, variability, and trends. Elem Sci Anth, 6, 10.

Zhang Y, Cooper OR, Gaudel A, et al. Tropospheric ozone change from 1980 to 2010 dominated 492 by equatorward redistribution of emissions. Nature Geosci, 2016, 9: 875-879 493

Ziemke, J. R., Chandra, S., & Bhartia, P. K. (2005). A 25-year data record of atmospheric ozone in the Pacific from Total Ozone Mapping Spectrometer (TOMS) cloud slicing: Implications for ozone trends in the stratosphere and troposphere. *Journal of Geophysical Research: Atmospheres*, *110*(D15).

Ziemke, J. R., L. D. Oman, S. A. Strode, A. R. Douglass, M. A. Olsen, R. D. McPeters, P. K. Bhartia, L. Froidevaux, G. J. Labow, J. C. Witte, A. M. Thompson, D. P. Haffner, N. A. Kramarova, S. M. Frith, L. K. Huang, G. R. Jaross, C. J. Seftor, M. T. Deland, and S. L. Taylor, Trends in global tropospheric ozone inferred from a composite record of TOMS/OMI/MLS/OMPS

1252 satellite measurements and the MERRA-2 GMI simulation, Atmos. Chem. Phys., 19, 3257-3269,
1253 https://doi.org/10.5194/acp-19-3257-2019, 2019.

1254 Ziemke, J. R., S. Chandra, B. N. Duncan, L. Froidevaux, P. K. Bhartia, P. F. Levelt, and J. W.
1255 Waters, Tropospheric ozone determined from Aura OMI and MLS: Evaluation of measurements
1256 and comparison with the Global Modeling Initiative's Chemical Transport Model, J. Geophys.
1257 Res., 111, D19303, doi:10.1029/2006JD007089, 2006.

1258

1259 Supplementary table-1: Primary volatile organic compounds. BIGALKANE is a lumped species
1260 for all alkanes C4 and greater, BIGENE lumps all alkenes C4 and greater.

S.N.	VOCs name
1	Benzene
2	BIGALKANE
3	BIGENE
4	acetylene
5	ethene
6	ethanol
7	ethane
8	propene
9	propane
10	formaldehyde
11	acetaldehyde
12	acetone
13	acetic acid
14	methanol
15	methane
16	formic acid
17	butan-2-one
18	toluene
19	xylenes

1261